Integration of phase-field model and crystal plasticity for the prediction of process-structure-property relation of additively manufactured metallic materials

Liu, P.W.
Wang, Z.
Xiao, Y.H.
Lebensohn, Ricardo A.
Liu, Y.C
Horstemeyer, Mark F.
Cui, X.Y
Chen, L

To be published in: International Journal of Plasticity

DOI to publisher's version: 10.1016/j.ijplas.2020.102670

Permalink to record: http://permalink.lanl.gov/object/view?what=info:lanl-repo/lareport/LA-UR-19-31422

Integration of phase-field model and crystal plasticity for the prediction of process-structure-property relation of additively manufactured metallic materials

P.W. Liu[a,b], Z. Wang[b,c], Y.H. Xiao[b,c], R.A. Lebensohn[d], Y.C. Liu[b], M.F. Horstemeyer[b,e], X.Y. Cui[a,*], L. Chen[b,c,*]

[a] *State Key Laboratory of Advanced Design and Manufacturing for Vehicle Body, Hunan University, Changsha, 410082, PR China*

[b] *Department of Mechanical Engineering, Mississippi State University, MS 39762, USA*

[c] *Department of Mechanical Engineering, University of Michigan-Dearborn, MI 48128-1491, USA*

[d] *Theoretical Division, Los Alamos National Laboratory, Los Alamos, NM 87845, USA*

[e] *School of Engineering, Liberty University, VA 24515, USA*

Abstract

A computational framework is developed to investigate the process-structure-property relationship for additive manufacturing (AM) of Ti-6Al-4V alloy. The proposed model incorporates experimentally informed two-phase α+β morphologies within prior β-grains, which are widely observed in the as-built AM components. Specifically, the temperature-dependent phase-field model (PFM) is used to simulate the evolution of various grain morphologies, e.g., columnar and equiaxed grain structures. The proposed PFM taking into account both of the epitaxial grain growth and the constitutional cooling-driven heterogeneous nucleation enables us to capture the columnar to equiaxed transition (CET) of grain structures. The thermal fields concerned with the scanning strategies and manufacturing parameters are simulated using a finite-element model (FEM). The Burgers orientation relation (BOR) is further utilized to generate two-phase α+β morphologies within prior β-grains, accompanied by the transformation of crystal orientations, i.e., $(0001)_\alpha//\{101\}_\beta$ and $<11\bar{2}0>_\alpha//<111>_\beta$. Finally, a fast Fourier transform-based elasto-viscoplastic (EVP-FFT) model is employed to predict the micromechanical behaviors and properties for the two-phase α+β microstructures. The presented PFM-based formulation is generally applicable to predict the process-structure-property relationship for additive manufacturing of a variety of alloy systems, e.g., titanium alloys, aluminum alloys and nickel-based superalloys.

Keywords: Phase-field model; Crystal plasticity; Elasto-viscoplasticity; Two-phase microstructure; Additive manufacturing.

---

[*] Corresponding author. Phone number: +1-662-325-3260; Fax Number: +1-662-325-7173;
E-mail Address: leichn@umich.edu (Lei Chen), cuixy@hnu.edu.cn (Xiangyang Cui)

1. Introduction

Additive manufacturing (AM) is a process by which materials are fabricated through an incremental method rather than by removal methods, offering great design flexibility, cost-effectiveness, and capability for delivering parts with complicated geometries. Therefore, AM processing is considered as a technique that can potentially revolutionize the manufacturing industry.

Titanium alloys have been successfully extended to many advanced applications, especially in the aerospace industry (Liu et al., 2016; Williams and Starke, 2003) and biomedical field (Harun et al., 2018; Sidambe, 2014), owing to their outstanding combinations of high specific strength, excellent fracture toughness and corrosion resistance.

In recent years, enormous experimental efforts (Keist and Palmer, 2016; Khan et al., 2012; Khan and Yu, 2012; Qiu et al., 2015) have been invested on additively manufactured titanium alloys, especially for the two-phase Ti-6Al-4V alloy. During AM process, due to the high energy inputs, steep thermal gradient is formed near the melt pool, usually leading to large columnar β-grain structures parallel to the building direction. The prior β-grain structures then undergo diffusionless β → α' martensitic transformation because of the high cooling rate. The acicular α' phase is generally transformed to lamellar α+β microstructures during the multiple thermal cycles (Xu et al., 2015). Consequently, a wide spectrum of α+β microstructures, ranging from acicular α', fully laminar α+β structures (or basket-weave and Widmanstätten structures), to combinations of the latter, can be obtained at the sub-grain level. Recent experiments show that the two-phase α+β microstructure plays an important role in the mechanical properties, such as elastic modulus, tensile strength, fracture strength, and ductility. (Al-Bermani et al., 2010) have found a highly columnar prior β-grain structure that, upon cooling, further transformed into an α+β microstructure during AM fabrication of Ti-6Al-4V. Low building temperature was beneficial for improving the microstructures and resultant mechanical properties. For example, once the building temperature exceeded 951 K, the yield strength decreased significantly due to the evidently coarsened colony size and thickness of α-lath. (Facchini et al., 2009) have found a very fine and stable α+β microstructure during AM fabrication of Ti-6Al-4V. This fine as-built microstructure has been proved to enhance yield strength and ultimate tensile strength, whilst improving the elongation at fracture. (Wang et al., 2016) have reported that very fine α+β microstructure was only observed in the thin wall, exhibiting high micro-hardness values and improved mechanical properties.

Considering the high yield strength and ductility imparted by fine α+β microstructure, numerous modeling techniques (Katzarov et al., 2002; Malinov and Sha, 2005; Murgau, 2016; Murgau et al., 2012) have been developed, in an attempt to explore the formation mechanisms of α+β microstructure in titanium alloys. (Chen et al., 2018) have modeled the β → α+β phase transformation during AM of Ti-6Al-4V using a hybrid finite-element and cellular automaton framework. They demonstrated that the α- and β-laths become thinner with increasing scanning speed, resulting from the higher cooling rates. (Baykasoglu et al., 2018) have investigated the evolution of Widmanstätten colony, fractions of α- and β-phases and α-lath thickness during AM of Ti-6Al-4V using an FE-based thermal-microstructural modeling approach. At the fourth layer, the high temperature β-phase would fully transform to basket-weave and Widmanstätten colony with volume fractions of 86% and 14%, respectively, in which the volume fraction of α-phase reached 91%, and the thickness of α-lath was 1.1 μm. (Klusemann and Bambach, 2018) have used a Johnson-Mehl-Avrami-Kolmogorov (JMAK) kinetics-based microstructural model to calculate the evolution of different phases under cyclic thermal loading during laser metal deposition of Ti-6Al-4V. The different temperature histories had insignificant influence on the final volume fractions of α- and β-phases, massive and martensite α-phase after five thermal cycles. The fine α-lath thickness was obtained under high temperature history for laser AM process. These modeling studies analyzed the process of β → α phase transformation and, to some extent, revealed the formation mechanisms of different α+β microstructures during AM of Ti-6Al-4V. However, they focused specifically on the development of α- and β-phases morphologies at the sub-grain level, thus failing to account for the effect of processing conditions on prior β-grain structures. Further, there is a lack of fundamental knowledge on the mechanical anisotropy of as-built parts associated with various microstructural features of the two-phase structure.

On the other hand, numerous attempts (Ji et al., 2017; Sahoo and Chou, 2016; Zhang et al., 2019) have been made to reveal the process-structure relationship of AM metals. For example, (Yan et al., 2018b, 2017) have explored the effect of powder bed on the heat transfer, melt pool dimension and porosity of building parts using an integrated discrete element method and computational fluid dynamics (CFD) method. They pointed out that, to a large extent, the input energy and powder layer thickness determined the quality of as-built products during metallic powder bed-based AM. Our group (Liu et al., 2019a) has investigated the thermal responses of aircraft engine blade during AM fabrication of Ti-6Al-4V alloy by using a well-tested "Tri-Prism" finite element method (TP-FEM). We have also developed a 2D computational model (Liu et al., 2018), coupling FE-based thermal model and phase-field model (PFM), to understand the formation mechanisms of site-specific β-grain structures during multi-layer AM fabrication of Ti-6Al-4V. This model provided the rationale for the formation of large vertical columnar $<001>_{\beta}//N_z$ grain structures and slanted inward grain structures by introducing grain nucleation, grain selection, layer-by-layer building fashion and grain epitaxial growth. To study the columnar to equiaxed transition (CET) of grain structures in metallic AM, we have developed a 3D grain growth phase-field model (Liu et al., 2019b) by taking the heterogeneous nucleation into account. The heterogeneous nucleation, due to the constitutional supercooling, impeded the growth of columnar β-grains and thus induced the equiaxed β-grains. Three-dimensional grain growth has also been simulated by (Wei et al.,

2019) during multi-layer laser AM of Inconel 718 using a Monte Carlo method-based grain growth model. They found that the cyclic heating and cooling had a great influence on grain growth, especially for the grain sizes and shapes.

Considerable numerical investigations (Bonatti and Mohr, 2017; Bronkhorst et al., 2019; Tancogne-Dejean et al., 2016) have also been performed in an attempt to understand the structure-property relation for metallic AM fabrication. (Ge et al., 2019) have studied the process-structure-property relationship in laser deposition melting of duplex titanium alloy, using an integrated FEM, Monte Carlo model and self-consistent model. They found that the predicted flow stresses were higher in the middle of printed parts but lower near the top or bottom surfaces. (Yan et al., 2018a) have also investigated the process-structure-property relationship during AM of Ti-6Al-4V alloy, using an integrated thermal-CFD model, cellular automation (CA) model and self-consistent clustering analysis (SCA). The melting and solidification of the powders and the resultant β-grain structures were well analyzed by the coupled thermal-CFD and CA models. The anisotropic stress-strain curves and fatigue crack were also predicted roughly. However, these computational framework failed to either predict the micromechanical fields or consider the sub-grain structures of Ti-6Al-4V formed by solid-state phase transformation. In recent years, (Lebensohn et al., 2012) have extended the fast Fourier transform (FFT)-based formulation for deformation of polycrystals in the elasto-viscoplastic regime (EVP). The EVP-FFT formulation has been well tested to predict the local micromechanical fields and effective mechanical behavior of heterogeneous materials (Tari et al., 2018). In engineering applications, it has been used for the structure-property analyses of dual phase Ti-6Al-4V by (Ozturk and Rollett, 2018), in which the experimental image-based microstructure was generated artificially. Other effective physics-based models have also been presented for simulations of mechanical responses. For example, (Mandal et al., 2017) have studied the plastic deformation of Ti-5Al-5Mo-5V-3Cr alloy using a self-consistent viscoplastic (VPSC) model. (Zhang et al., 2007) have investigated the slip behaviors and quasi-static stress-strain responses of duplex Ti-6Al-4V based on the polycrystalline finite element simulations. (Kochmann et al., 2018, 2016) have predicted the effective material behavior of polycrystals using a two-scale FE-FFT-based computational model. However, either the synthetic grain structures or image-based sub-grain morphology was used as input to predict the mechanical behavior with these models. The relationship of process-microstructure-property for metallic AM fabrication, especially the physically-informed two-phase α+β microstructure within grains, has not been well investigated.

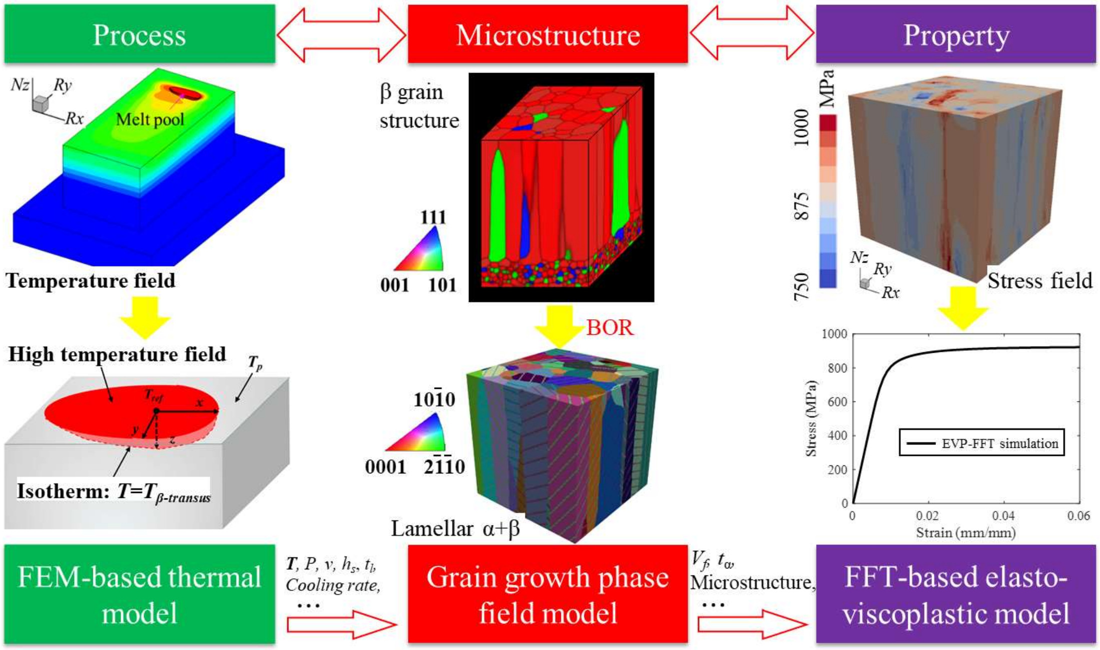

Fig. 1. Schematic of the proposed computational framework to investigate the process-microstructure-property relationship of AM-fabricated metallic material. Some directly relative parameters/ variables that required to be transferred between different models are listed. They include high temperature field $\boldsymbol{T}$, beam power P, scanning speed v, hatching space h_s, layer thickness t_l, cooling rate, volume fraction of α-phase V_f, α-lath thickness t_α and lamellar α+β microstructure and so on.

In this study, a computational framework, integrating FEM, grain growth PFM and EVP-FFT calculation, is thus presented here, as shown in Fig. 1. The proposed model provides the systematic investigation of process-microstructure-property relationship during AM fabrication of Ti-6Al-4V alloy and firstly incorporates experimentally informed two-phase lamellar α+β morphologies within prior β-grains. The EVP-FFT model improves the computational efficiency of crystal plasticity and predicts accurately micromechanical behavior and properties of AM-built lamellar α+β microstructures. The FEM is utilized to simulate the thermal responses controlled by scanning strategies and processing conditions during AM at the macroscale, and the extracted thermal information is then input into a temperature-dependent PFM to model the evolution of various 3D grain morphologies, *i.e.*, large columnar and equiaxed β-grain structures and textures. These prior β-grain structures are considered as a parent phase, which, upon cooling, gradually transforms into acicular α' martensite and/ or lamellar α+β phases. Given the typical characteristics of two-phase Ti-6Al-4V at the ambient temperature, fully lamellar α+β microstructures are generated. The transformation of crystal orientations from β → α phases is performed, based on the Burgers orientation relation (BOR) (Zhang et al., 2007), i.e., $(0001)_{\alpha}//\{101\}_{\beta}$ and $<11\bar{2}0>_{\alpha}//<111>_{\beta}$. Grain morphologies, pole figures and effective mechanical behavior of as-printed Ti-6Al-4V components are studied in detail using the presented computaional framework.

2. Finite-element based 3D thermal model

In the rapid solidification process of additive manufacturing, thermal information, such as temperature distribution, temperature history and thermal gradient, plays a critical role in tailoring grain evolution at the mesoscale. (DebRoy et al., 2018) have illustrated that the non-uniform temperature field inside the melt pool lead to a surface tension gradient that acted as a driving force for the flow of molten metal. (Antonysamy et al., 2013) have found that grains epitaxially grew along the direction of maximum thermal gradient, perpendicular to the curved surface of melt pool, resulting in large columnar $<001>_{\beta}//N_z$ grain structures. Therefore, a FE-based heat transfer simulation at the ABAQUS 2018 platform (Systèmes, 2018) is first conducted to obtain the 3D melt pool and high temperature field near the melt pool under different processing conditions. A typical schematic of powder bed-based electron beam melting (EBM) process is plotted in Fig. 2a. The powders are spread out firstly each layer. Then the electron beam scans with pre-defined contours in the successive powder layers to fabricate the printed part. This procedure is repeated consecutively until the final product is completed.

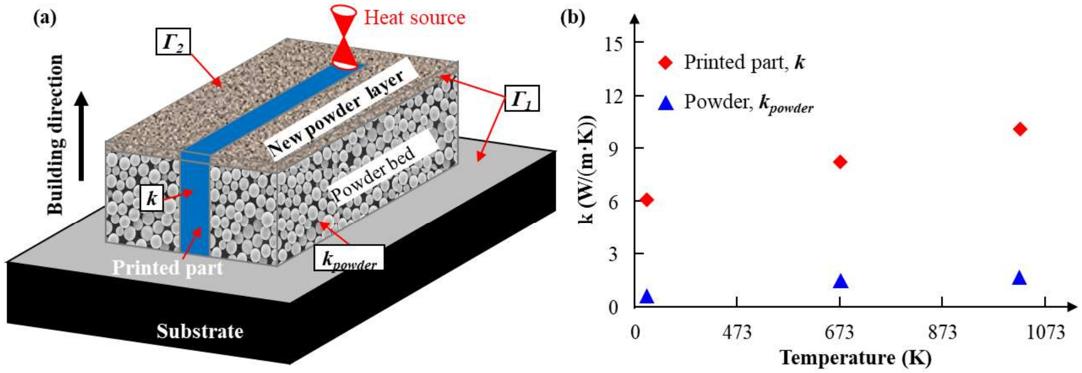

Fig. 2. (a) A typical schematic of powder bed-based electron beam melting process. Γ_1 shows the domain on which Dirichlet boundary condition is applied. The convection and radiation boundary conditions are applied on the top surface of the printed parts Γ_2. (b) plots the thermal conductivities of the printed part k and powders k_{powder} at different temperature.

The transient heat conduction equation accompanying with a body heat flux is given as follows:

$$\frac{\partial}{\partial x}\left(k\frac{\partial T}{\partial x}\right)+\frac{\partial}{\partial y}\left(k\frac{\partial T}{\partial y}\right)+\frac{\partial}{\partial z}\left(k\frac{\partial T}{\partial z}\right)+\rho Q_e=\frac{\partial\left(\rho H\left(T\right)\right)}{\partial t}, \qquad (1)$$

where $T(x, y, z, t)$ is the tempo-spatial temperature field as a function of time (t) and position (x, y, z), ρ is temperature-dependent density, k, thermal conductivity, is plotted in Fig. 2b. It is noted that the thermal conductivity of powders, ~ 1.0 W/(m ·K), is negligible in this study as it is much smaller than that of printed parts. $H(T)$ denotes the enthalpy per unit mass that incorporates the latent heat of phase transformation during the melting and solidification. In a single phase zone, $H(T)$ is defined up to a constant by specific heat $C_p = \mathrm{d}H/\mathrm{d}T$ of the phase. In the two phase mushy zone, $H(T)$ is the mass-weighted average of the $H(T)$ of the individual phases. Q_e, body heat flux, models the moving heat source. It consists of a surface Gaussian distribution and a penetration depth of electron beam (Raghavan et al., 2016):

$$Q_e = \eta \cdot P \cdot \frac{4\ln(0.1)}{\pi d^2 l_e} \cdot \exp\left(\frac{4\ln(0.1)(x^2+y^2)}{d^2}\right) \cdot \left(-3\left(\frac{z}{l_e}\right)^2 - 2\left(\frac{z}{l_e}\right) + 1\right), \quad (2)$$

where η is the absorption efficiency, P is the power of electron beam calculated by acceleration voltage U_e and beam current I_e, d is the electron beam diameter, l_e is the absolute penetration depth of electron beam derived by the following equation in powder bed-based EBM of Ti-6Al-4V (Jamshidinia et al., 2013):

$$l_e = 2.1 \times 10^{-5} \times \frac{U_e^2}{\rho}, \quad (3)$$

For powder bed-based EBM process, the powder layer should be sintered before melting to prevent the splash of powders. Therefore, the substrate and powder layers, Γ_1, are preheated with a preheating temperature T_P. The convection and radiation boundary conditions are applied on the top surface Γ_2 of the printed parts due to the high temperature near the melt pool, which can be described as follows:

$$-k\frac{\partial T}{\partial x}n_x - k\frac{\partial T}{\partial y}n_y - k\frac{\partial T}{\partial z}n_z = h(T - T_a), \qquad \textit{Convection boundary for } \mathbf{x} \textit{ on } \Gamma_2, \quad (4a)$$

$$-k\frac{\partial T}{\partial x}n_x - k\frac{\partial T}{\partial y}n_y - k\frac{\partial T}{\partial z}n_z = \varepsilon_R \sigma_R (T^4 - T_a^4), \textit{ Radiation boundary for } \mathbf{x} \textit{ on } \Gamma_2, \quad (4b)$$

where T_a is the ambient temperature, h = 10.0 W/m^{2}K, $\varepsilon_R = 0.49$ and $\sigma_R = 5.67 \times 10^{-8}$ W/m^{2}K^4 are heat convective coefficient, emissivity and Stefan-Boltzmann constant, respectively. The processing parameters (Liu et al., 2018) used in the thermal model for Ti-6Al-4V alloy are given in Table 1. The temperature-dependent material parameters, i.e., density, specific heat and thermal conductivity of Ti-6Al-4V (Jamshidinia et al., 2013), at specified temperatures are calculated by the following cubic polynomial (Liu et al., 2018), $a_0 + a_1T + a_2T^2 + a_3T^3$, where a_0, a_1, a_2 and a_3 are fitting coefficients. These values are listed in Table 2.

Table 1
Processing parameters of the thermal model.

Processing parameters (units)	Symbol	Value

Electron beam acceleration voltage (kV)	U_e	60.0
Electron beam current (mA)	I_e	6.0~12.0
Scanning speed (m/s)	v	0.4~3.0
Absorption efficiency	η	0.8
Preheating temperature (K)	T_p	993.0
Electron beam diameter (μm)	d	200.0
Layer thickness (μm)	t_l	100.0
Hatching space (mm)	h_s	0.1
Component length (mm)		38.1
Component height (mm)		5.0
Substrate height (mm)		6.35
Substrate width (mm)		38.0
Substrate length (mm)		76.2

Table 2
Coefficients for density, specific heat and conductivity of Ti-6Al-4V.

Material properties	a_0	a_1	a_2	a_3
Specific heat/ W/(m·K)	531.1	0.1185	1.883×10^{-5}	-7.921×10^{-9}
Conductivity/ J/(kg·K)	4.968	4.973×10^{-3}	8.044×10^{-6}	-2.008×10^{-9}
Density/ kg/m^3	4.652×10^{3}	-0.9391	9.255×10^{-4}	-3.133×10^{-7}

3. Phase-field model for grain growth

Phase-field method has been developed by (Krill III and Chen, 2002; X. Wang et al., 2019) to simulate the dendrite growth and grain structure evolution. As the phase-field method does not explicitly track the interface positions, it can dramatically reduce the computational costs and is used for large scale modeling, especially three-dimensional simulations. In this work, we extend our previous 2D model (Liu et al., 2018) to 3D using similar fundamental theories. A sequence of phase variables $\{\Phi_q(\boldsymbol{r},\ t)\}$ are used to obtain the grain structure and crystallographic orientation of each grain in the whole simulation domain. The total free energy of the polycrystalline material is given as follows:

$$F(t)=\int\left[w\cdot f_e\left(\phi_1(\mathbf{r},t),\phi_2(\mathbf{r},t),\ldots,\phi_Q(\mathbf{r},t)\right)+\sum_{q=1}^{Q}\frac{\kappa_q}{2}\left(\nabla\phi_q(\mathbf{r},t)^2\right)\right]d\mathbf{r}, \tag{5}$$

in which, w is the barrier height, κ_q is the positive gradient energy coefficient associated with the grain boundary energy, $f_e(\{\Phi_q(\boldsymbol{r},\ t)\})$ represents the local free energy density given by the following expression:

$$f_e\left(\left\{\phi_q(\mathbf{r},t)\right\}\right)=-\frac{a}{2}\sum_{q=1}^{Q}\phi_q^2(\mathbf{r},t)+\frac{b}{4}\left(\sum_{q=1}^{Q}\phi_q^2(\mathbf{r},t)\right)^2 +\left(c-\frac{b}{2}\right)\sum_{q=1}^{Q}\sum_{s>q}^{Q}\phi_q^2(\mathbf{r},t)\phi_s^2(\mathbf{r},t), \tag{6}$$

where a, b and c are constants with $a = b = c = 1$ for grain growth (Krill III and Chen, 2002).

3.1 Temperature-dependent grain evolution

For AM fabrication of Ti-6Al-4V, the 3D grain evolution in time and space is obtained by solving the time-dependent Ginzburg-Landau equations:

$$\frac{\partial\phi_q(\mathbf{r},t)}{\partial t}=-L_q(T)\frac{\delta F(t)}{\delta\phi_q(\mathbf{r},t)}\quad(q=1,2,\ldots,Q), \tag{7}$$

where $L_q(T)$ is the temperature-dependent kinetic rate coefficient defined by the modified Arrhenius type equation (Ataibis and Taktak, 2015; Ohno et al., 2013):

$$L_q(T)=L_0^*\cdot\left(\frac{T}{T_a}\right)^m\cdot\exp\left(-\frac{\Delta E}{R_g T}\right), \tag{8}$$

in which, L_0^* and m ($-1<m<1$) are constants, $R_g = 8.314$ J/(mol·K) is the gas constant, ΔE is the activation energy with the value of 97.0 KJ/mol for Ti-6Al-4V alloy (Gil and Planell, 2000). It is noted that Eq. (8) is a link to bridge the macroscopic thermal model and mesoscopic phase-field model. On the other hand, in the 3D grain growth modeling, we mainly focus on the prior β-grain structures and textures formed when temperature exceeds β-transus temperature, $T_{\beta\text{-}transus}$. Thus, the stable 3D melt pool and high temperature field enclosed by the isotherm $T=T_{\beta\text{-}transus}$ near the melt pool, see Fig. 1, are required and further substituted into Eq. (8) at each grid point to curb the kinetic rate coefficients dictating grain boundary evolution. They are updated every 10 printing layers (1 mm). In this process, a linear interpolation scheme (Shewchuk, 2002) is used to achieve the temperature of each grid point in the PFM simulation due to ~7 times difference in mesh size between the FE-based thermal model and grain growth PFM.

3.2 Heterogeneous nucleation

Heterogeneous nucleation, originating from the addition of nucleant particles and/or constitutional supercooling, essentially induced by solute segregation, can facilitate grain refinement during rapid solidification of metals. (Martin et al., 2017) have found that improving the heterogeneous nucleation by adding ZrH_2 nanoparticles as nucleant promotes equiaxed grain structures and high-strength aluminium alloys during AM. (Schempp et al., 2014) have reported that a constitutionally supercooled zone was formed in the solute-enriched liquid ahead of the solid/liquid (S/L) interface.

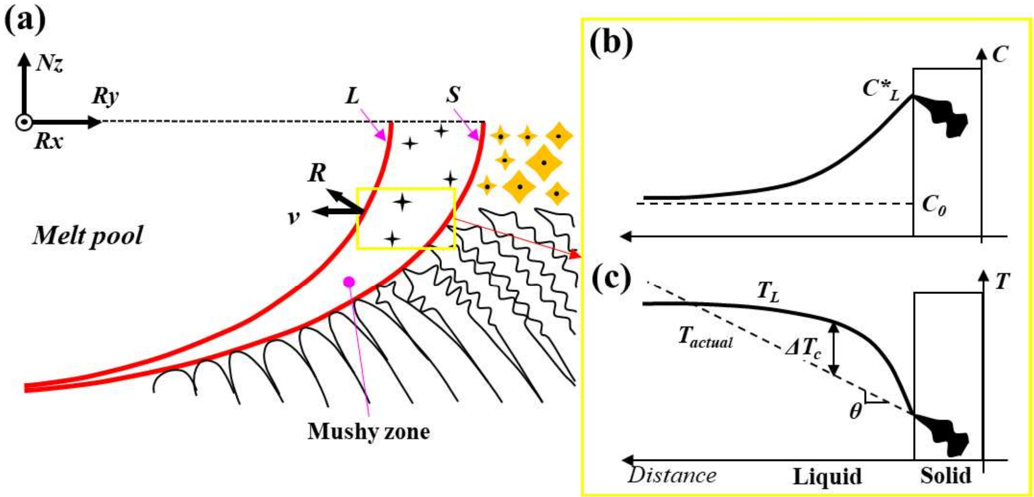

Fig. 3. (a) Schematic of grain nucleation and growth near the melt pool. v and R are scanning speed of electron beam and solidification rate, respectively, L and S represent liquidus and solidus. The mushy zone involves both liquid and solid phases, (b) and (c) plot the hypothetical solute concentration and corresponding temperature profile near the S/L interface. The horizontal axis describes the distance from the grain front along solidification direction. θ, the slope of the line of actual temperature, is equal to the thermal gradient.

As shown in Fig. 3a, grain growth induced by constitutional supercooling can be either in an epitaxial manner or attributed to heterogeneous nucleation. The dominance of each mechanism significantly depends on the spatially localized solute and temperature field near the melt pool, as illustrated in Fig. 3b and c. Since the solute accumulate at the front of grains, liquidus temperature gradually decreases as the solute diffuses near the S/L interface. This results in constitutional supercooling ΔT_c, defined by the difference between liquidus temperature and actual temperature, which is an important factor contributing to heterogeneous nucleation in rapid solidification processes (Liu et al., 2019b). By considering the thermal undercooling ΔT_t because of the solidification latent heat and the curvature undercooling ΔT_r, the total undercooling ΔT is given by Eq. (9) as follows:

$$\Delta T = \Delta T_c + \Delta T_t + \Delta T_r , \tag{9}$$

In this study, to obtain the equiaxed grain structures, an extreme scanning strategy, *i.e.*, high scanning speed and low electron beam power, is adopted in spite of the porosity defect, which provides a large constitutional supercooling and a high nucleation probability. More detailed illustrations about the calculations of undercooling and heterogeneous nucleation probability are given in our previous work (Liu et al., 2019b).

3.3 Two-phase lamellar α+β microstructure

The prior β-grain structures then gradually transform into the lamellar α+β microstructures as the temperature T is below $T_{\beta\text{-transus}}$. (Tan et al., 2015) have reported that the microstructure was composed of the lath-like α-phase with the hexagonal close packed (HCP) structures and β-phase with body centered cubic (BCC) structures, *i.e.*, lamellar α+β microstructures, at the ambient temperature, as shown in Fig. 4b. The typical lamellar α+β microstructures have also been widely observed by (Al-Bermani et al., 2010; Chen et al., 2019; Edwards et al., 2019; Facchini et al., 2009) during AM fabrication of Ti-6Al-4V alloy, and exhibited higher mechanical performance than the traditional microstructure with primary α’ martensite formed in heat treatment (Filip et al., 2003; Gil et al., 2003; Sieniawski et al., 2013). In this study, the artificial microstructures with the successive parallel α- and β-laths in each prior β-grain, as illustrated in Fig. 4d, are generated in a theoretically rigorous way, and utilized as input of the EVP-FFT calculation. This procedure involves two aspects: (1) to generate the successive α- and β-laths within each prior β-grain, and (2) to assign crystal orientations for α- and β-phases, as demonstrated in Section 3.3.1 and Section 3.3.2, respectively.

3.3.1 To generate the successive α- and β-laths within each prior β-grain

We first create the successive parallel α- and β-laths within each parent β-grain, in which a random α-variant is selected from the 12 variants in β → α phase transformation. Fig. 4d plots a simulated 3D lamellar α+β microstructure with α-lath thickness of 2.0 μm, α-volume fraction (V_f) of 87.5% and β-volume fraction of 12.5%. Once α-variant is selected, we can determine a series of parallel planes that are perpendicular to the crystal plane indices, i.e., Miller indices, of the selected α-variant. The region between two planes with a distance of α-lath thickness t_α is defined as the α-phase. Its adjacent regions with a distance of t_β are defined as the β-phases, as shown in Fig. 4c and d. The volume fractions of α- and β-phases are roughly controlled by the ratio of the thicknesses of α- and β-laths. This procedure is conducted on the platform of MTEX tool in Matlab (Mainprice et al., 2011).

3.3.2 To assign crystal orientations for α- and β-phases

Crystal orientation is an important parameter in both phase transformation and crystal plastic deformation. Previous literature (Crawford and Chawla, 2009; Schwarzer and Gerth, 1993) has illustrated two ways to describe the crystal orientation, *i.e.*, Miller indices and Euler angles, which possess a corresponding relation for the specific crystal structure and specimen coordinate. In this study, the Bunge Euler angles (φ_1, Φ, φ_2) (Socrates, 2003) are used to describe the crystallographic texture. The color is defined by the RGB values that are derived from the Bunge Euler angles, as given by Eq. (10):

$$\begin{aligned} Red &= 255\cdot\frac{\varphi_1}{360}, 0\le\varphi_1\le 360^{\circ} \\ Green &= 255\cdot\frac{\phi}{180}, 0\le\phi\le 180^{\circ}\,. \\ Blue &= 255\cdot\frac{\varphi_2}{360}, 0\le\varphi_2\le 360^{\circ} \end{aligned} \tag{10}$$

Here, the red, green and blue colors represent the <001>/<0001>, <101>/$<2\bar{1}\bar{1}0>$ and <111>/$<10\bar{1}0>$ orientations, respectively.

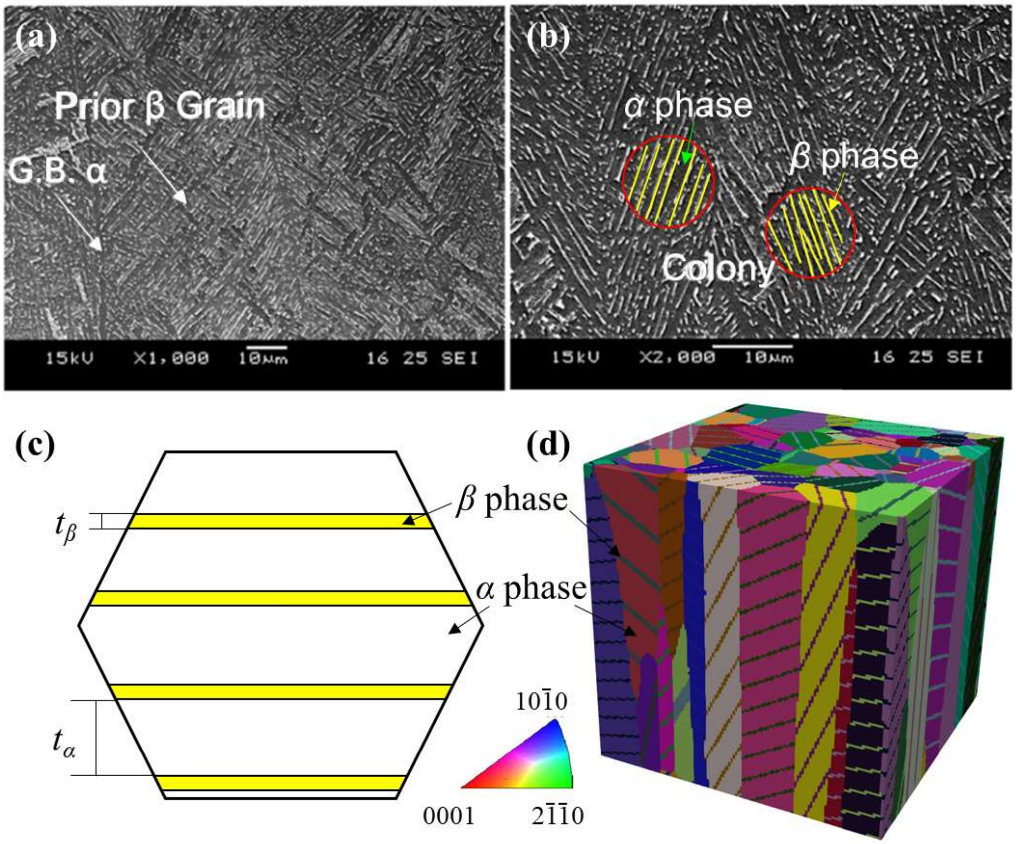

Fig. 4. (a) and (b) show the scanning electron microscope (SEM) results (Tan et al., 2015), including the columnar prior β-grains and colony morphologies, i.e., lamellar α+β microstructures within prior β-grains. As α-phase was etched out by Kroll's reagent, it exhibits dark contrast while β is in bright under SEM mode; (c) demonstrates a representative schematic of the lamellar α+β microstructure, which is composed of the successive parallel α- and β-phases. t_α and t_β are the thicknesses of α- and β-laths; (d) a simulated 3D lamellar α+β microstructure.

In PFM modeling, a random orientation is assigned when heterogeneous nucleation occurs. Then, these nuclei grow competitively to give the final high-temperature prior β-grains with a specific Bunge Euler angles, i.e., crystal orientation. In the β → α phase transformation, the Bunge Euler angles of each prior β-grain are employed to deduce the 12 α-variants, based on the Burgers orientation relation, designated $(0001)_\alpha//\{101\}_\beta$ and $<11\bar{2}0>_\alpha//<111>_\beta$. Once α-variant is selected, the Miller indices and corresponding Bunge Euler angles of the α-phase are determined. Then, the color of each α-lath is calculated using the Bunge Euler angles by Eq. (10), as shown in Fig. 4d. The orientation of the retained β-phase may be the same with that of the parent β-phase or belong to the same family of crystal planes.

4. EVP-FFT micromechanical model

4.1 FFT-based elasto-viscoplastic formulation

The FFT-based elasto-viscoplastic formulation has been reported in detail in previous literature (Lebensohn et al., 2012). Therefore, only the fundamental aspects of this approach are presented here. For more details, see Ref. (Lebensohn et al., 2012).

EVP-FFT provides an exact solution of the governing differential equations of stress equilibrium and strain compatibility in a periodic unit cell. The lamellar α+β microstructure is obtained from the previously described grain growth PFM simulation mapped onto a regularly-spaced grid $\{\mathbf{x}_\mathrm{d}\}$. A corresponding grid of the same dimensions is employed in Fourier space $\{\xi_\mathrm{d}\}$. An average strain rate $\dot{E}_{ij} = (V_{i,j} + V_{j,i})/2$, defined by the average velocity gradient $V_{i,j}$, is imposed on the unit cell.

For elasto-viscoplastic problems in the infinitesimal-strain setting, the strain field, involving elastic strain $\boldsymbol{\varepsilon}^e(\mathbf{x})$ and viscoplastic strain $\boldsymbol{\varepsilon}^p(\mathbf{x})$, is defined as:

$$\boldsymbol{\varepsilon}(\mathbf{x}) = \boldsymbol{\varepsilon}^e(\mathbf{x}) + \boldsymbol{\varepsilon}^p(\mathbf{x}). \tag{11}$$

By using the Hooke's law and Euler implicit time discretization, Eq. (11) can be further rewritten as follows:

$$\boldsymbol{\varepsilon}(\mathbf{x}) = \mathbf{C}^{-1}(\mathbf{x}) : \boldsymbol{\sigma}(\mathbf{x}) + \boldsymbol{\varepsilon}^{p,t}(\mathbf{x}) + \dot{\boldsymbol{\varepsilon}}^p(\mathbf{x})\Delta t. \tag{12}$$

The local constitutive relation between the plastic strain rate $\dot{\boldsymbol{\varepsilon}}^p(\mathbf{x})$ and the stress $\boldsymbol{\sigma}(\mathbf{x})$ at a single crystal material point $\mathbf{x}$, is given by a rate-dependent crystal plasticity approach:

$$\dot{\boldsymbol{\varepsilon}}^p(\mathbf{x}) = \sum_{s=1}^{N} \mathbf{m}^s(\mathbf{x}) \dot{\gamma}^s(\mathbf{x}) = \dot{\gamma}_0 \sum_{s=1}^{N} \mathbf{m}^s(\mathbf{x}) \left(\frac{\left| \mathbf{m}^s(\mathbf{x}) : \boldsymbol{\sigma}(\mathbf{x}) \right|}{\tau^s(\mathbf{x})} \right)^n \operatorname{sgn}\left(\mathbf{m}^s(\mathbf{x}) : \boldsymbol{\sigma}(\mathbf{x}) \right), \tag{13}$$

where $\dot{\gamma}^s(\mathbf{x})$ and $\dot{\gamma}_0$ are the shear rate and normalization factor, respectively, $\mathbf{m}^s(\mathbf{x})$ represents the Schmid tensor of slip system (s) at point $\mathbf{x}$, $\tau^s(\mathbf{x})$ is the critical resolved shear stress (CRSS) associated with the accumulated plastic strain in the crystal, n is a stress exponent.

A polarization field is defined by considering the stress tensor and stiffness of a reference linear medium $\mathbf{C}^0$:

$$\varphi_{ij}(\mathbf{x}) = \sigma_{ij}(\mathbf{x}) - C^0_{ijkl}(\mathbf{x}) u_{k,l}(\mathbf{x}) = \sigma_{ij}(\mathbf{x}) - C^0_{ijkl}(\mathbf{x}) \varepsilon_{kl}(\mathbf{x}), \tag{14}$$

where $u_{k,l}(\mathbf{x})$ is the displacement gradient tensor. Combining Eq. (14) with the equilibrium equation $\sigma_{ij,j}(\mathbf{x}) = 0$:

$$C^0_{ijkl}(\mathbf{x}) u_{k,lj}(\mathbf{x}) + \varphi_{ij,j}(\mathbf{x}) = 0 . \tag{15}$$

The differential Eq. (15) for a unit cell with periodic boundary conditions can be solved using the Green function method. With the periodic Green function $G_{km}(\mathbf{x})$ associated with the displacement field $u_k(\mathbf{x})$, the solution of displacement gradient can be obtained as the convolution integral between derivatives of the Green function and the polarization field:

$$u_{k,l}(\mathbf{x}) = \int_{R^3} G_{ki,jl}(\mathbf{x} - \mathbf{x}') \varphi_{ij}(\mathbf{x}') d\mathbf{x}' . \tag{16}$$

Using the convolution theorem, Eq. (16) can be solved in Fourier space. The compatible strain field, including macroscopic and local strains, is given by:

$$\varepsilon_{ij}(\mathbf{x}) = E_{ij} + \mathrm{FT}^{-1}\left(sym\left(\hat{\Gamma}^0_{ijkl}(\boldsymbol{\xi})\right) \hat{\varphi}_{kl}(\boldsymbol{\xi}) \right), \tag{17}$$

in which, the symbol "^" and "FT^{-1}" denote the Fourier transform and its inverse transformation, respectively, $\boldsymbol{\xi}$ is a frequency point in Fourier space, the Green operator in Fourier space $\hat{\Gamma}^0_{ijkl}(\boldsymbol{\xi}) = -\xi_j \xi_l \hat{G}_{ik}(\boldsymbol{\xi})$ is a function of the reference stiffness tensor and the frequency, where $\hat{G}_{ik}(\boldsymbol{\xi}) = \left[C^0_{kjil} \xi_l \xi_j \right]^{-1}$.

Equation (17) is a fix-point equation for the strain field that allows solving the constative and governing equations iteratively. In practice, for better convergence of our micromechanical model for AM microstructures, we use a modified version of the above algorithm, based on the augmented Lagrangian formulation of (Michel, J. C., H. Moulinec, 2000), adapted to the EVP polycrystals (see (Lebensohn et al., 2012) for details).

4.2 Hardening law – Voce model for two-phase microstructure

Due to the strain hardening, the evolution of the threshold stress τ^s is a function of the total accumulated shear strain $\Gamma(\mathbf{x}) = \sum_{t=1}^{N_t} \sum_{s=1}^{N} \dot{\gamma}^s(\mathbf{x}, t)\Delta t$, in which N_t is the number of time increments. To describe the relationship between τ^s and Γ, an extended Voce law is used, as in (Tome et al., 1984) and (Lebensohn et al., 2007), with the following form:

$$\tau^s(\Gamma) = \left(\tau_0^*\right)^s + \left(\tau_1^s + \theta_1^s \Gamma\right)\left(1 - \exp\left(-\Gamma \left|\frac{\theta_0^s}{\tau_1^s}\right|\right)\right), \tag{18}$$

where θ_0 and θ_1 are the initial and asymptotic hardening rates, respectively, $(\tau_0 + \tau_1)$ refers to the back-extrapolated stress. The initial yield stress, τ_0^*, is governed by α-lath thickness, t_α, via the Hall-Petch relationship (Körner, 2016):

$$\tau_0^* = \tau_0 + 101.4 \cdot t_\alpha^{-0.5}, \tag{19}$$

where the coefficient of 101.4 MPa·μm$^{0.5}$ is adopted from experimental measurement (Körner, 2016). The elastic constants of BCC and HCP phases and hardening parameters used for Voce model are listed in Table 3 and Table 4, respectively. In this study, to simplified calculation, the parameters of hardening law in each point, i.e., τ_0, τ_1, θ_0 and θ_1, are the weighted average values of the two phases according to the volume fraction. It is noted that the τ^s, used in Eq. (18), does not depend on the temperature and loading rate. However, despite that, this equation has been widely used in crystal plasticity models primarily because of its simplicity and ease of calibration.

Table 3

Elastic constants of BCC and HCP phases for Ti-6Al-4V alloy (Ozturk and Rollett, 2018).

Elastic constants (GPa)	C_{11}	C_{12}	C_{13}	C_{33}	C_{44}
BCC	130	90	90	130	65
HCP	143	110	90	177	40

Table 4

Voce hardening parameters for different slip systems (Ozturk and Rollett, 2018; Tari et al., 2018).

Hardening parameters (MPa)	τ_0	τ_1	θ_0	θ_1
BCC	41.09	99.62	971.27	1.6
HCP (basal)	184.95	5.0	1160.0	-18.9
HCP (prismatic)	264.21	5.0	1160.0	-18.9
HCP (pyramidal)	792.63	5.0	1160.0	-18.9

5. Results and discussions for AM fabrication of Ti-6Al-4V alloy

5.1 Investigation of process-structure relationship

5.1.1 Grain structures and textures

This section aims to demonstrate the ability of the present model to reproduce the experimentally observed two-phase α+β morphologies within prior β-grains. In the grain growth PFM, the layer-by-layer printing fashion is explicitly taken into account. Periodic boundaries are applied to the 3D simulation domain with a size of 2.0 × 2.0 × 5.0 mm^3. A substrate with the pre-existing fine equiaxed grain structures mimics the “starter plate” for building up the layers during AM fabrication of Ti-6Al-4V alloy. With the movement of high temperature field enclosed by the isotherm of $T=T_{\beta\text{-transus}}$, grains in general grow epitaxially along the maximum thermal gradient direction, leading to the well-known columnar grain structures. However, once the sufficient constitutional supercooling or heterogeneous nucleation occurs, the equiaxed grains are formed near the centerline of the melt pool gradually and interrupt the columnar grain growth, thereby giving rise to the CET of grain structures, as illustrated in Fig. 3.

Fig. 5a and b show the simulated β-grain structures and textures for the AM-fabricated Ti-6Al-4V alloy under two processing conditions (PC 1 and PC 2). Under PC 1 with P = 480 W and v = 0.4 m/s, a very low constitutional supercooling is developed, resulting in the limited heterogeneous nucleation and thus the formation of large columnar β-grain structures, as demonstrated in Fig. 5a. These columnar β-grains extend across multiple building layers from the substrate. Under PC 2, with an ameliorative scanning strategy of P = 360 W and v = 3.0 m/s, the small electron beam power and high scanning speed facilitate the heterogeneous nucleation to obtain the fine equiaxed β-grain structure, since this processing condition gives rise to the large constitutional supercooling at the S/L interface (Liu et al., 2019b). The achieved 3D fine equiaxed β-grain structure is shown in Fig. 5b. In the first several layers, the ratio between the thermal gradient *G* and the solidification rate *R*, i.e., an important indicator of the solidification patterns (Liu et al., 2018; Schempp et al., 2014), is large due to cold substrate, thus producing columnar grains. On the contrary, the ratio *G*/*R* becomes much smaller away from the substrate, indicating high nucleation probability. These nuclei suppress the epitaxial growth of columnar grains, and thus resulting in fine equiaxed β-grain structures. The extremely high scanning speed, however, may lead to the lack of fusion of powders, inducing porosity defects.

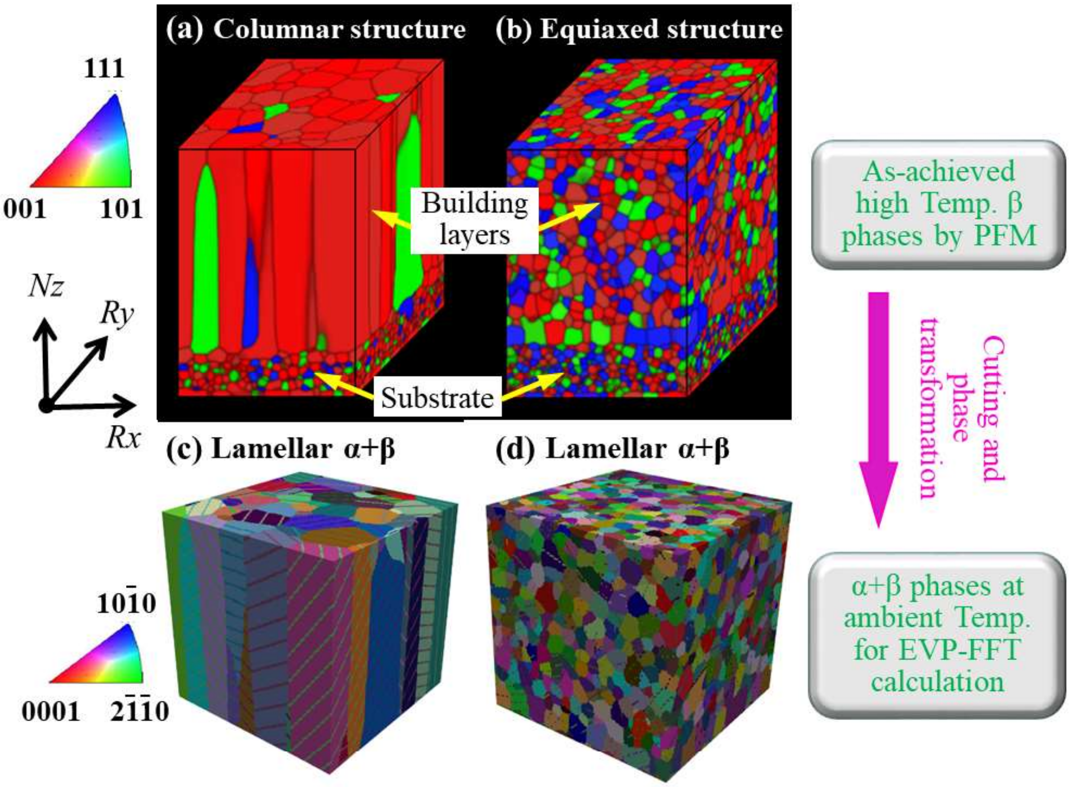

Fig. 5. 3D β-grain morphologies, involving (a) columnar grains and (b) equiaxed grains. (a) and (b) display the results simulated by the grain growth phase-field model under processing condition 1 and processing condition 2, respectively; (c) and (d) display the transformed lamellar α+β microstructures that are cut directly from (a) and (b), respectively, and then used for EVP-FFT calculations.

The strong $<001>_{\beta}//N_z$ fiber textures, see Fig. 5a, are observed in this simulation under

PC 1. This can be explained by two main reasons. First, the <001> axis of BCC crystal is the preferred growth direction, inherently ascribed to the anisotropy in its thermal conductivity, elastic modulus and surface energy (Antonysamy, 2012; Lee et al., 1997). Second, grains also prefer to grow along the maximum thermal gradient at the solidification front. Therefore, in the case of elongated melt pool and thus thermal gradient approximately along N_z-direction, these grains with <001> or quasi-<001> orientations, visualized by the red color, as shown in Fig. 5a, possess optimal alignment of its <001> axis along thermal gradient. This brings them the strongest grain growth and thus the final dominance over the domain. For the equiaxed β-grain textures, see Fig. 5b, we can clearly see that the number of grains with <101> and <111> orientations increases substantially due to the heterogeneous nucleation with various orientations.

Fig. 5c and d show the simulated lamellar α+β microstructures under PC 1 and PC2, respectively. The cubic representative volumes are directly cut off the as-obtained grain structures from PFM, i.e., Fig. 5a and b, and retains the original regularly-spaced meshes. These prior β-grains then transform to the two-phase α+β microstructures upon cooling, as demonstrated in Section 3.3. Owing to the higher beam power and lower scanning speed of PC 1, the cooling rate under PC 1 is significantly smaller than that of PC 2. Thus, the α-lath thickness of 1.72 μm under PC 1, see Fig. 5c, is much larger than 0.26 μm (Scharowsky et al., 2015) under PC 2, see Fig. 5d. In contrast, the volume fraction of the α-phase is about 87.45% under PC 1, which is lower than 94.02% under PC 2. This trend is consistent with experimental observations (Scharowsky et al., 2015), in which the thickness of α-lath decreases with increasing scanning speed due to the high cooling rate.

5.1.2 Effect of process parameters on β-grain morphologies

In order to demonstrate the relationship between process and microstructure, we performed systematic simulations with varying solidification rate R and thermal gradient G, by manipulating scanning strategies and manufacturing parameters (Liu et al., 2019b), during AM fabrication of Ti-6Al-4V alloy.

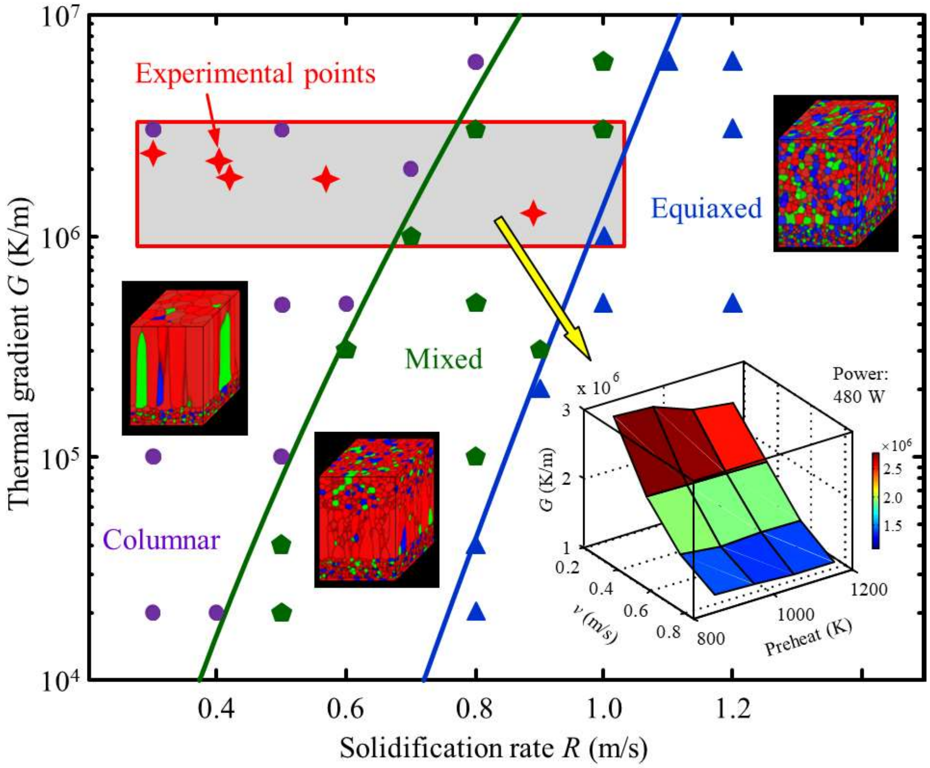

Fig. 6. Diagram showing the transition of β-grain structures as a function of the solidification rate R and the thermal gradient G. Two fitted boundary lines from computational data points represented by the symbols, with purple, dark green and blue colors, divide the grain-structure region into three different zones, i.e., columnar, mixed and equiaxed zones, respectively. The red rectangle shows the ranges of solidification parameters, i.e., thermal gradient and solidification rate, with the common experimental conditions. The inserted 3D plot shows the simulated thermal gradient in the range of $1.0 \sim 3.0 \times 10^6$ K/m under the printing conditions of $P = 480$ W, v: 0.2 ~ 0.8 m/s, T_P: 873 ~1200 K. The red shurikens display the experimental data for AM-built Ti-6Al-4V taken from Refs. (Al-Bermani et al., 2010; Antonysamy et al., 2013; Juechter et al., 2014; Rafi et al., 2013a; Tan et al., 2015).

Fig. 6 shows a “phase diagram” that quantifies the transition of grain structures as a function of the solidification rate R and thermal gradient G. The G-R space is divided into three zones, *i.e.*, columnar, mixed and equiaxed zones, by the two fitted boundary lines from computational data points. The grain aspect ratio λ, i.e., the ratio of grain length to width, is selected to describe the three grain structures. Specifically, $\lambda > 6$ represents the columnar β-grains, $6 > \lambda > 2$ for the mixed β-grains, and $\lambda < 2$ for the equiaxed β-grains. The boundaries of the "phase diagram" suggest that a higher *R* and a lower *G* promote the development of equiaxed β-grain structures. In contrast, at a lower *R* and a lager *G*, the columnar β-grain structures are favored. The red rectangle shows the ranges of solidification parameters, i.e., thermal gradient and solidification rate, with the common experimental conditions. The common experimental conditions are those where electron beam power ranges from 120 W to 900 W, scanning speed is 0.2 ~ 1.0 m/s, preheating temperature is 800 ~ 1200 K (Al-Bermani et al., 2010; Antonysamy, 2012; Antonysamy et al., 2013; Cheng et al., 2014). The red shurikens display the experimental data for AM-built Ti-6Al-4V taken from Refs. (Al-Bermani et al., 2010; Antonysamy et al., 2013; Juechter et al., 2014; Rafi et al., 2013a; Tan et al., 2015).

This "phase diagram" provides a guideline to tailor the β-grain morphologies by optimizing the manufacturing conditions. As shown in the inserted 3D plot in Fig. 6, increasing the preheating temperature and/or improving the scanning speed are effective ways to reduce the thermal gradient, thus enabling the development of equiaxed β-grain structures under common AM conditions. However, it is still costly to achieve sufficiently small thermal gradient by excessively increasing preheating temperature. Meanwhile, the extremely high scanning speed might lead to undesired lack-of-fusion porosity induced by insufficient power density. Therefore, a balance between manufacturing parameters and defects should be made to achieve the desirable microstructures.

Note that some other parameters can influence this "phase diagram". For example, we have recently studied the relative influence of various physical and material parameters on grain structures (Z. Wang et al., 2019a, 2019b). Global sensitivity analysis shows that the grain structures are most sensitive to density and grain boundary energy. In the current study, we mainly focus on the effect of processing parameters, i.e., beam power, scanning speed and preheating temperature, on grain morphologies during AM of Ti-6Al-4V. Those three parameters are usually what manufacturer directly control in practice and are the most used ones in AM parametric study. However, if needed, the presented multiscale multi-physics model can be easily extended to parametric study of some other parameters (e.g., physical and material parameters) in terms of similar phase diagrams.

5.2 Investigation of microstructure-property relationship

5.2.1 Anisotropic mechanical behaviors of columnar β-grain structures

In this section, the anisotropic mechanical behavior, attributed to the large columnar grain morphologies from the AM fabrication of Ti-6Al-4V, are studied using the EVP-FFT model. A PFM-simulated columnar β-grain structure, see Fig. 5a, is obtained firstly under PC 1, and then transformed into the lamellar α+β microstructure upon cooling, as shown in Fig. 5c. The procedure of β → α phase transformation has been demonstrated in Section 3.3. As discussed by (Scharowsky et al., 2015), the relationship between the thickness of α-lath t_α and volume energy E_v is approximate linear under different processing conditions, i.e., $t_\alpha = 0.01349 \cdot E_v + 0.09783$. In addition, the E_v is defined as $E_v = P/(v \cdot h_s \cdot t_l)$, where P is the beam power, v is the scanning speed, h_s is the hatching space and t_l is the layer thickness. Therefore, in this study, the thickness of α-laths is set as 1.72 μm under the processing condition 1, i.e., $P = 480$ W, $v = 0.4$ m/s. The volume fractions of α- and β-phases are 87.45% and 12.55%, respectively. The 3D cubic simulation domain is discretized into the 128×128×128 grids, and a periodic boundary condition is applied on the simulation domain. The uniaxial tension are implemented along N_z- and R_x-direction for anisotropic analysis. The effective stress-strain curves are plotted in Fig. 7, which illustrates a clear difference in mechanical response for tension applied along different directions. The strengths in N_z- and R_x-directions are 891.7 MPa and 922.0 MPa, respectively, reaching a difference of 30.3 MPa that is close to the experimental measurement of 30 ± 7.2 MPa (Rafi et al., 2013a).

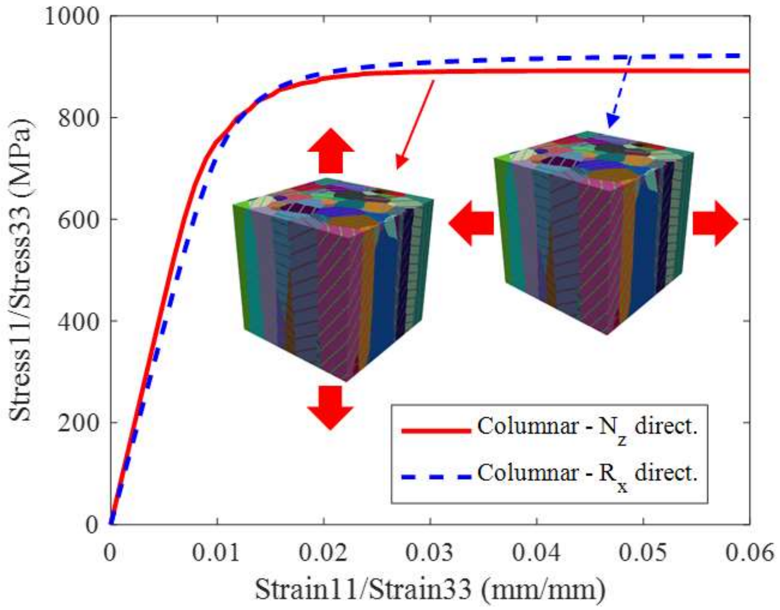

Fig. 7. Anisotropic mechanical properties of the large columnar grain structures under the processing condition 1.

(a) Strain 33 **(b) Stress 33**

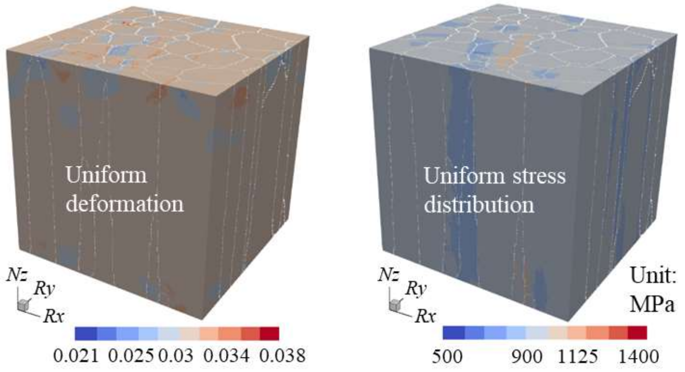

(c) Strain 11 **(d) Stress 11**

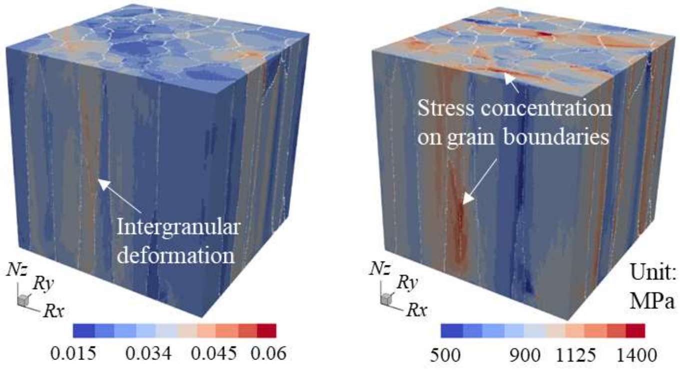

Fig. 8. Micromechanical fields predicted in the large columnar grain structures under the processing condition 1. The white lines describe the grain boundaries. (a) and (b) show the strain and stress fields with tension applied along N_z-direction; (c) and (d) show the strain and

stress fields with tension applied along R_x-direction.

The strain fields, including elastic and plastic strains, are shown in Fig. 8a and c with tension along N_z- and R_x-directions, respectively. The strain field for N_z-direction stretching is more uniform than that of R_x-direction stretching. From Fig. 8c, we can clearly see that the intergranular deformation stands out, while deformation within a grain is relatively homogeneous. Stress concentrations mainly appear between grains in R_x-direction stretching, as demonstrated in Fig. 8d, while the stress distribution is uniform when loading along N_z-direction, as shown in Fig. 8b. Its maximum stress is no more than 1100 MPa, which is far less than that of 1400 MPa with tension applied along R_x-direction.

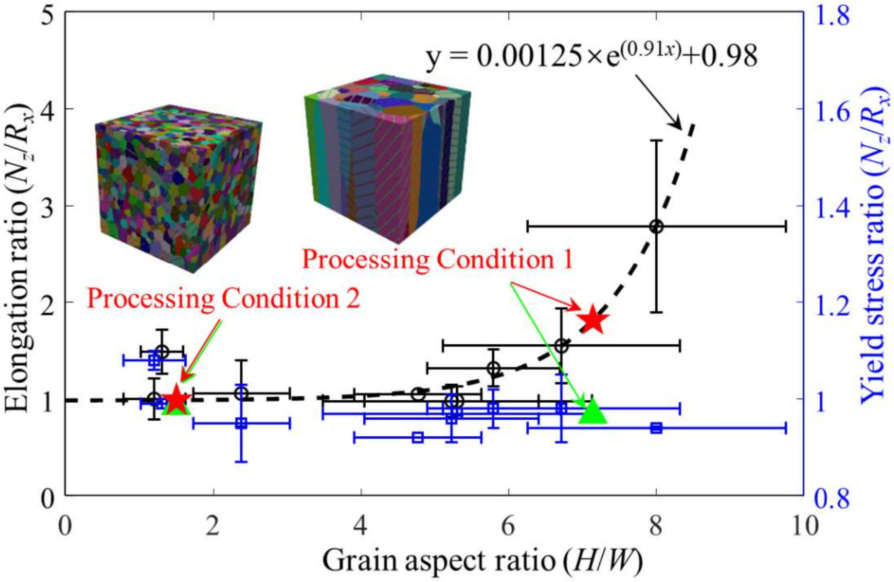

Fig. 9. Elongation and yield stress ratios (N_z-direction/R_x-direction), marked by black circles and blue squares, respectively, versus grain aspect ratio (grain height, *H*/width, *W*) for tests performed in Wilson's study (Wilson-Heid et al., 2017) as well as data from literature (Carroll et al., 2015; Keist and Palmer, 2016; Palanivel et al., 2016; Qiu et al., 2013; Rafi et al., 2013a, 2013b; Zhao et al., 2016). A fitted function, manifested by the black dotted curve, is obtained from the experimental data, which is further used to calculate the elongation ratios, marked by red stars, using the simulated grain aspect ratios under Processing Condition 1 and 2 (PC 1 and PC2). The green triangles demonstrate the simulated yield stress ratios under PC 1 and PC 2.

To quantitatively analyze the relationship between anisotropic microstructure and ductility as well as mechanical property in AM fabrication of Ti-6Al-4V, the elongation and yield stress ratios versus grain aspect ratio are plotted in Fig. 9. The black dotted line is a fitted result from the experimental measurements (Carroll et al., 2015; Keist and Palmer, 2016; Palanivel et al., 2016; Qiu et al., 2013; Rafi et al., 2013a, 2013b; Wilson-Heid et al., 2017; Zhao et al., 2016), from which it can be concluded that when the grain aspect ratio is less than about 6, i.e., equiaxed β-grain structures, there is no evident anisotropy in elongation, since isotropic grains dilute the impact of anisotropic ones. However, a significant anisotropic ductility is observed once the grain aspect ratio exceeds 6, i.e., columnar β-grain structures. It is believed that the dislocation can glide both along the entire length of grain boundaries and along the slip planes/bands with tension applied along N_z-direction, manifested by the homogeneous strain field, see Fig. 8a, that improve the resistance in fracture, enabling larger plastic deformation. When loading is applied along R_x-direction, the stress concentration tend to occur along the grain boundaries, which could result in the crack nucleation and propagation as the stress exceeds the ultimate strength of 978 MPa (Rafi et al., 2013a), and thus deteriorate the ductility of columnar β-grain structures in R_x-direction. The stress concentration might be attributed to the dislocation gliding just along grain boundaries, leading to dislocation pile-ups, manifested by the large plastic strain near the grain boundaries, see Fig. 8c. In this study, the grain aspect ratio under PC1 is 7.14, with a significant anisotropy in ductility, while ductility is isotropic for PC2, for which grain aspect ratio is 1.4.

Both experimental measurements and numerical modeling show the yield stress ratios are almost equal to 1, illustrating that the anisotropy in yield stress is not significant for β-grain morphologies, see the data of blue squares and green triangles in Fig. 9. It should be noted that this approach, where only β-grain aspect ratios are required, can be used for prediction of anisotropic ductility in AM of Ti-6Al-4V. The effect of sub-grain structures, like lamellar α+β and Widmanstätten, on ductility has not been considered here.

5.2.2 *Effect of grain structures on mechanical properties*

We subsequently explore the effect of grain morphologies on anisotropic mechanical property. The processing condition 2, contributing to promoting heterogeneous nucleation, is performed to achieve the fine equiaxed β-grain structures, as shown in Fig. 5b. Upon cooling, these fine equiaxed β-grain structures then transform to the lamellar α+β microstructure, see Fig. 5d, based on the Burgers orientation relation. The thickness of α-lath is 0.26 μm (Scharowsky et al., 2015) under PC 2, i.e., $P = 360$ W, $v = 3.0$ m/s. The volume fractions of α- and β-phases are 94.02% and 5.98%, respectively. This obtained lamellar α+β microstructure is employed as input of EVP-FFT simulations.

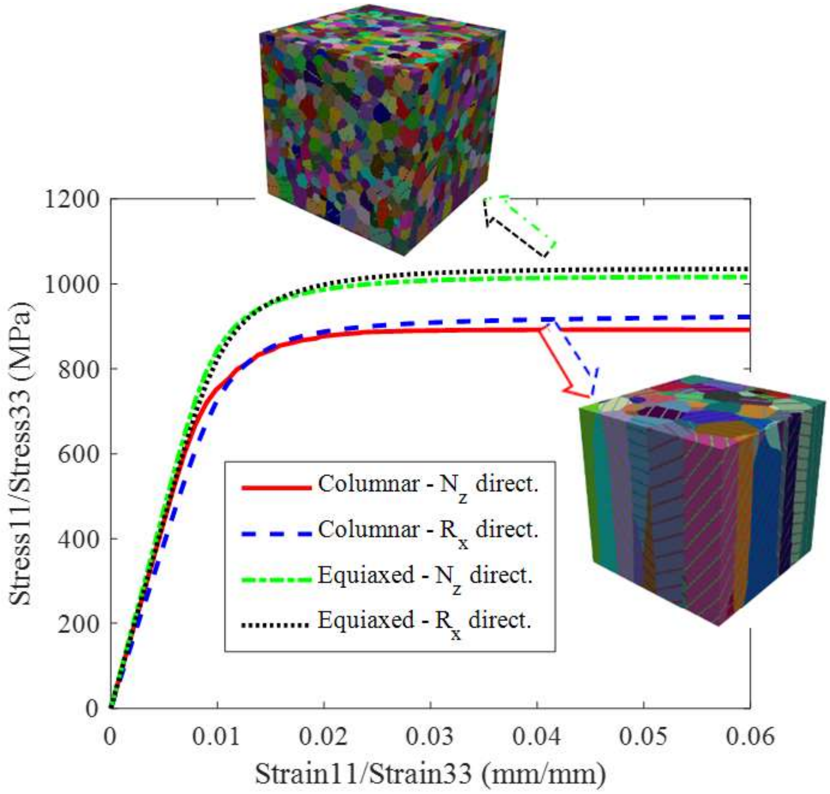

Fig. 10. Effect of different grain morphologies on mechanical properties.

Fig. 10 shows the stress-strain curves for columnar and equiaxed grain structures with tensions in N_z- and R_x-directions, which illustrates that different grain morphologies, *i.e.*, columnar and equiaxed grain structures, have a strong influence on the mechanical properties. Up to ~ 130 MPa difference in yield stress is achieved for these two different microstructures, see Fig. 5a and b, under the same loading conditions.

Fig. 11 depicts similar strain and stress fields with uniform distributions under the two different loading conditions. For equiaxed grain structures, stretching perpendicular to the grain boundaries dominates the deformation patterns due to nearly spherical grains. In addition, the distributions of grains along N_z- and R_x-directions are uniform. Therefore, the equiaxed grain structures provide isotropic mechanical behaviors rendering nearly the same mechanical responses with loading in different directions.

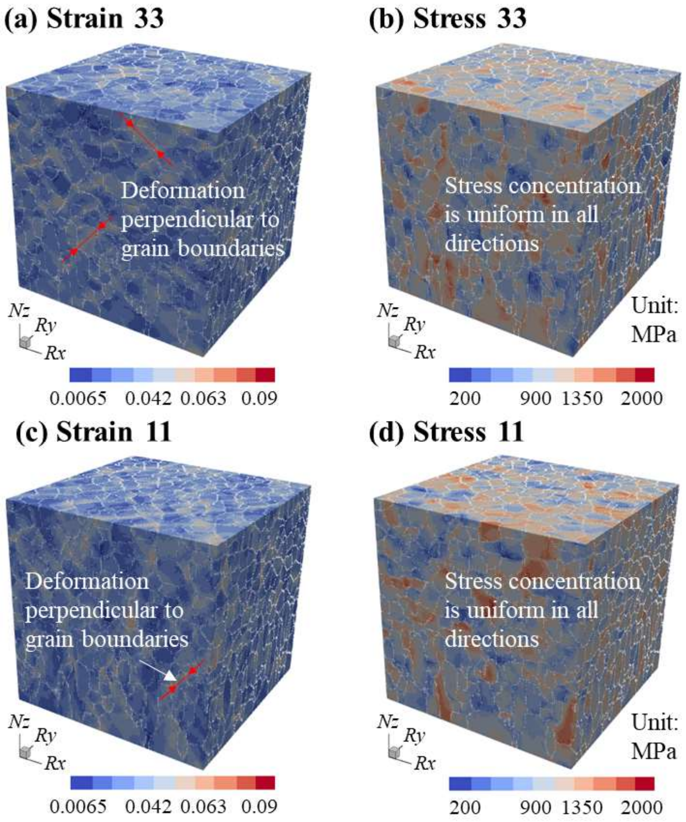

Fig. 11. Micromechanical fields for the equiaxed grain structures under the processing condition 2. The white lines describe the grain boundaries. (a) and (b) show the results with tension applied along N_z-direction; (c) and (d) show the results with tension applied along R_x-direction.

For two-phase Ti-6Al-4V alloy, the slip length, an important parameter that determines yield stress in plastic deformation of metals (Al-Bermani et al., 2010; Baufeld et al., 2011), heavily depends on the grain shapes of parent phases and α-lath thickness. As discussed before, the equiaxed grains have the smaller grain size and thinner α-lath thickness than that of columnar grains. The fine α-lath microstructures impede the movement of dislocation, and hence reduce the effective slip length, which further readily induce the dislocation pile-ups and improve the yield stress as well as the tensile strength. On the contrary, columnar grains might possess the longest effective slip length, especially for slipping in building direction. Therefore, the yield stress with loading along N_z-direction is smallest, as shown in Fig. 10.

5.3 Outlook for the computational framework

The current computational framework enables a systematic investigation on process-structure-property relationship during AM fabrication of Ti-6Al-4V alloy. It spans several orders of magnitude in length scale, i.e., macroscale (length scale is 1 mm), grain scale (length scale is 10 μm) and sub-grain scale (length scale is 10 nm ~ 1 μm). However, the current computational framework is still an early model. It is easy to combine with the sub-grain PFM (Ji et al., 2017) to model the real-time $\beta \rightarrow \alpha$ phase transformation upon cooling, and allows future integration with atomistic models (Fang et al., 2019) for incorporating more detailed dislocation movement and pile-up in predicting the micromechanical responds. In addition, the developed computational framework can be readily extended to the investigation of other alloy systems, e.g., aluminum alloys and nickel-based superalloys, for AM process.

6. Conclusions

A computational framework incorporating FE-based thermal model, grain growth PF model and EVP-FFT micromechanical model has been developed, and applied to the study of process-structure-property relationship during metallic additive manufacturing. The presented computational framework has been validated at each level through comparisons with experimental observations (Al-Bermani et al., 2010; Antonysamy et al., 2013; Facchini et al., 2009; Gil et al., 2003; Ozturk and Rollett, 2018; Sieniawski et al., 2013).

The process-structure-property relationship has been systematically studied in terms of AM-fabricated Ti-6Al-4V:

- Two-phase lamellar α+β morphologies within prior β-grains for Ti-6Al-4V alloy are considered in the current computational framework. A Voce hardening model, taking into account the volume fraction of α- and β-phases as well as the α-lath thickness, is employed to capture the mechanical responses of two-phase Ti-6Al-4V alloy.

- Low beam power and high scanning speed provide high probability of heterogeneous nucleation by improving constitutional supercooling, and thus promote the columnar to equiaxed transition of grain structures. Simultaneously, the high volume fraction of α-phase and fine α-lath are obtained due to the low volume energy input. On the contrary, the high beam power and low scanning speed fabricate the large columnar β-grain structures.
- Equiaxed β-grain structures have the smaller grain size and the shorter slip length, and thus provide much higher yield stress, up to ~ 130 MPa, than that of large columnar β-grain structures.
- Fine α-lath microstructure and small lamellar colony size reduce the effective slip length, prone to more dislocation pile-ups, and thus improves the yield stress and tensile strength of AM-built Ti-6Al-4V parts.
- For the columnar β-grain structures, the reduction of elongation in R_x-direction is attributed to a mass of stress concentration along the grain boundaries, which could result in the crack nucleation and propagation as the stress exceeds the ultimate strength of 978 MPa.

Acknowledgements

This work is financially supported by National Science Foundation of China (11872177), the Foundation for Innovative Research Groups of the National Natural Science Foundation of China (51621004), National Key R& D Program of China (2017YFB1002700), Hunan Provincial Innovation Project of Graduate Students (CX2017B081) and the China Scholarship Council. Z. Wang, Y.H. Xiao, L. Chen are grateful for the financial support by the program of ORAU Ralph E. Powe Junior Faculty Enhancement Award and NSF CMMI, United States (1662854). The computer simulations were carried out on the clusters of High Performance Computing Collaboratory (HPC^2) at Mississippi State University.

Appendix

A1. Validate the grain growth phase-field model

We first quantitatively validated the current grain growth PFM by comparing the simulated β-grain size distributions with the experimental results under PC 1, as listed in Table A1. It can be seen that the width of these simulated columnar grains lies within 0.173 - 0.448 mm, and their length ranges from 0.2 mm to 5.0 mm, extending through the entire printing height, which are in accordance with the experimentally measured width ranging from 0.15 mm to 0.3 mm and length in the range of 1.4 mm to 5.0 mm (Antonysamy, 2012).

Table A1
Experimental and statistical β-grain size distributions under processing condition 1.

β-grain sizes			
Experimental measurement (Ranges)		Statistical results (Ranges)	
Width (mm)	Length (mm)	Width (mm)	Length (mm)
0.150 - 0.300	1.400 - 5.000	0.173 - 0.448	0.200 - 5.000

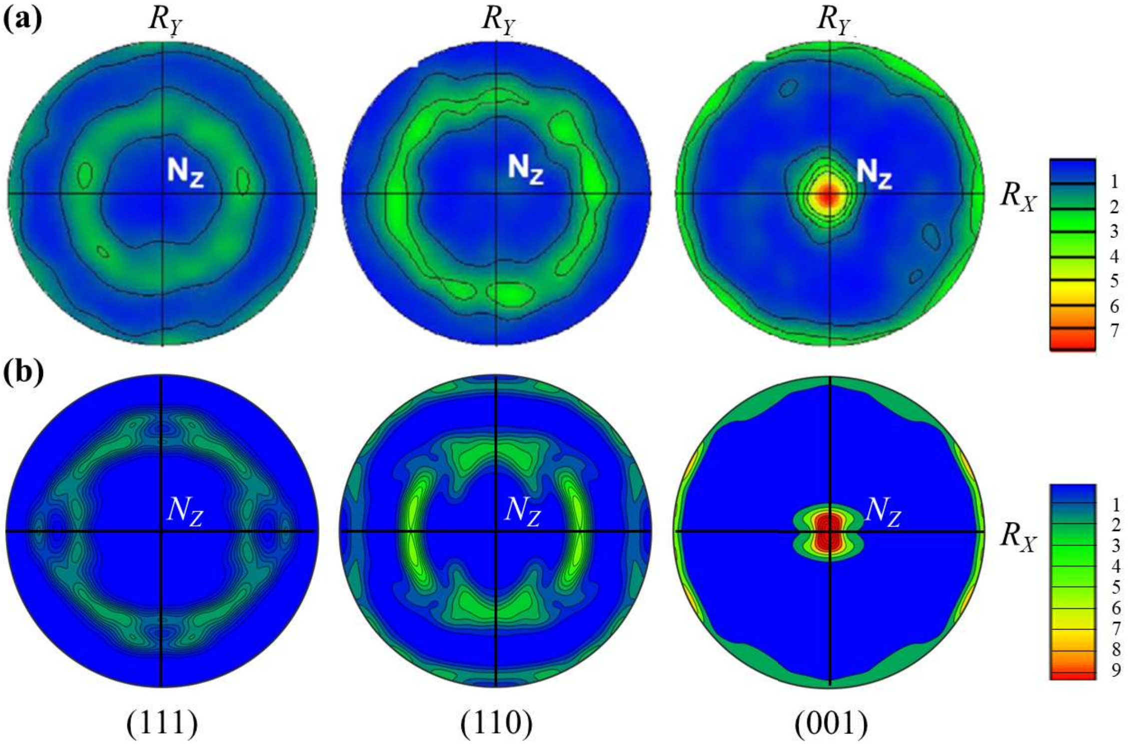

Fig. A1. Pole figures of columnar β-grain textures: (a) and (b) experimental measurements and simulation results, respectively, under processing condition 1.

Fig. A1 compares the pole figures, depicting the columnar β-grain textures, from the PFM simulations with experimental measurements under PC 1. Approximately 800 grains and 100 grains are utilized for texture analysis of the experiment and the computational modeling, respectively. Both experimental measurements (Antonysamy et al., 2013) and simulation results based on the MTEX tool in Matlab (Mainprice et al., 2011) imply a strong $<001>_\beta//N_z$ fiber texture. The distributions of $<101>_\beta$ and $<111>_\beta$ textures are reasonably uniform, and their intensity is much smaller than that of $<101>_\beta$ orientation. The maximum intensity of $<001>_\beta$ texture is ~ 8 times random in experimental observation (Antonysamy et al., 2013), while it is about 9 times random in simulation.

A2. Validate the fast Fourier transform-based elasto-viscoplastic (EVP-FFT) model

In this section, we further validated the proposed model by quantitatively predicting the mechanical properties of two-phase microstructures of Ti-6Al-4V alloy. The columnar prior β-grain structures and textures, consisting of 100 grains with random orientations, are firstly generated using Voronoi tessellation and then transformed into the lamellar α+β microstructure for micromechanical calculations. The simulation domain is discretized into a 128×128×128 grid. The elastic constants and hardening parameters of BCC and HCP phases are adopted from the literature (Ozturk and Rollett, 2018; Tari et al., 2018), as listed in Table 3 and Table 4. For the analysis of elasto-plastic deformation, the two-phase microstructure is composed of 88% α-phase with α-lath thickness of 1.7 μm and 12% β-phase, inspired by experimental measurements (Facchini et al., 2009; Scharowsky et al., 2015; Thomas et al., 2012). The uniaxial tension boundary condition is conducted along N_z-direction. The two-phase EVP-FFT simulation is carried out by applying a tensile strain of 6%, at a rate of 1.0 s^{-1}, as shown in Fig. A2. The stress-strain curve obtained from the two-phase EVP-FFT simulation agrees well with the experimental measurement by (Facchini et al., 2009) for the AM fabrication of Ti-6Al-4V alloy.

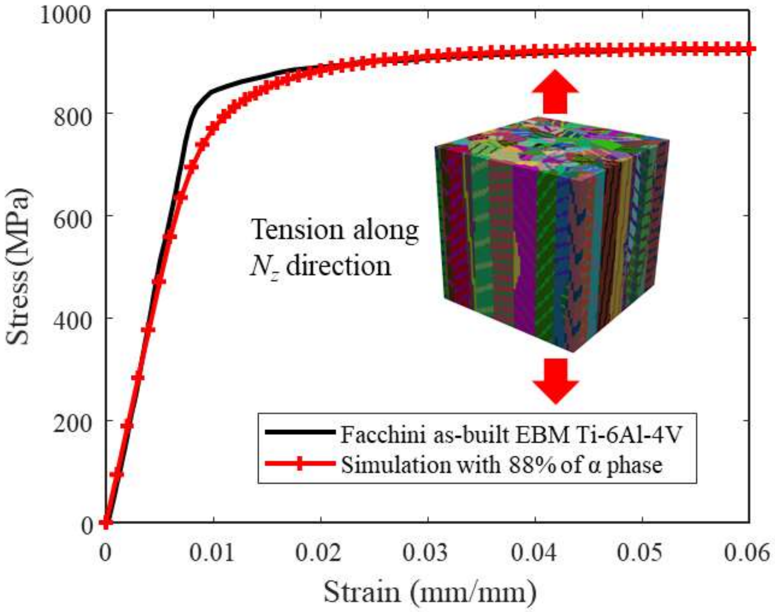

Fig. A2. Stress-strain curves corresponding to experiment (Facchini et al., 2009), and simulation using the proposed model.

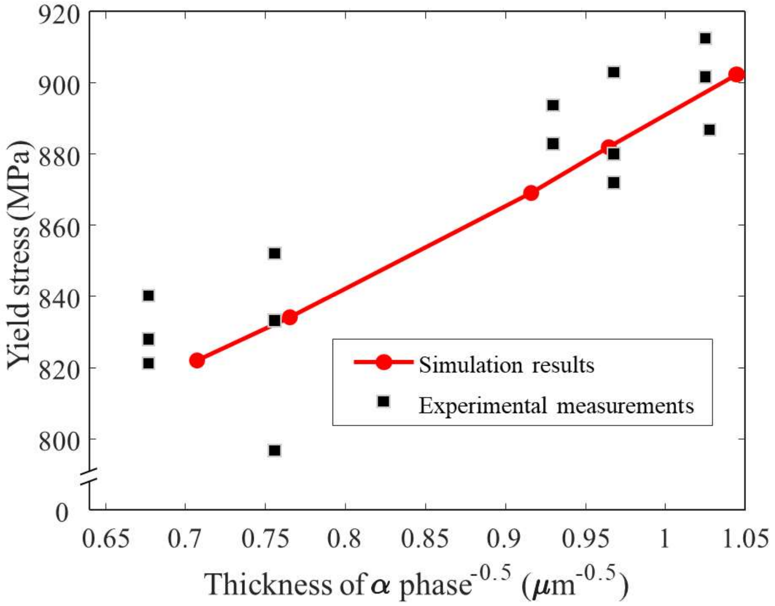

Fig. A3. Yield stress as a function of the inverse square root of α-lath thickness.

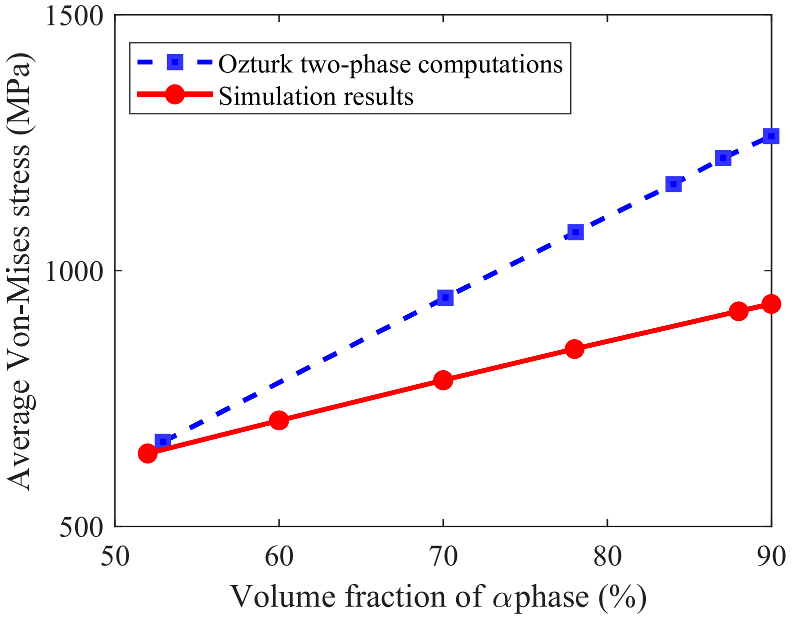

Fig. A4. Relationships between average Von-Mises stress and volume fraction of α-phase.

Mechanical properties of two-phase Ti-6Al-4V alloy depend strongly on the microstructural features of the particular phases. In the case of the lamellar α+β microstructure, the α-lath thickness, volume fraction of α-phase, α-colony size and β-grain size have the most significant influence (Filip et al., 2003; Sieniawski et al., 2013). To validate the two-phase EVP-FFT crystal plasticity predictions, the effects of α-lath thickness and volume fraction of α-phase on the mechanical properties of Ti-6Al-4V are investigated. The simulation results, as depicted in Fig. A3, demonstrate that there is a linear relationship between the yield stress and the inverse square root of the α-lath thickness, in accordance with the experimental measurements (Galarraga et al., 2017). Since the α-phase is harder than the β-phase, the averaged Von-Mises stress increases significantly with volume fraction of α-phase. The influence of volume fraction of α-phase for a dual-phase Ti-6Al-4V alloy has been studied by (Ozturk and Rollett, 2018) using a FFT-based elasto-viscoplastic micromechanical model. The difference of predicted stresses at different volume fraction of α-phase is acceptable, considering the uncertainty of various parameters in each model, such as α-lath thickness, grain size of colony, grain orientation distribution and so on. In spite of that, the linear increases of the averaged Von-Mises stresses with increasing volume fractions of α-phase are obtained in both of the simulations, as shown in Fig. A4.

REFERENCE

Al-Bermani, S.S., Blackmore, M.L., Zhang, W., Todd, I., 2010. The origin of microstructural diversity, texture, and mechanical properties in electron beam melted Ti-6Al-4V. Metall. Mater. Trans. A Phys. Metall. Mater. Sci. 41, 3422–3434. https://doi.org/10.1007/s11661-010-0397-x

Antonysamy, A.A., 2012. Microstructure , Texture and Mechanical Property Evolution during Additive Manufacturing of Ti6Al4V Alloy for Aerospace Applications. University of Manchester. https://doi.org/10.1007/s11665-013-0658-0

Antonysamy, A.A., Meyer, J., Prangnell, P.B., 2013. Effect of build geometry on the β-grain structure and texture in additive manufacture of Ti6Al4V by selective electron beam melting. Mater. Charact. 84, 153–168. https://doi.org/10.1016/j.matchar.2013.07.012

Ataibis, V., Taktak, S., 2015. Characteristics and growth kinetics of plasma paste borided Cp-Ti and Ti6Al4V alloy. Surf. Coatings Technol. 279, 65–71. https://doi.org/10.1016/j.surfcoat.2015.08.023

Baufeld, B., Brandl, E., Van Der Biest, O., 2011. Wire based additive layer manufacturing: Comparison of microstructure and mechanical properties of Ti-6Al-4V components fabricated by laser-beam deposition and shaped metal deposition. J. Mater. Process. Technol. 211, 1146–1158. https://doi.org/10.1016/j.jmatprotec.2011.01.018

Baykasoglu, C., Akyildiz, O., Candemir, D., Yang, Q., To, A.C., 2018. Predicting Microstructure Evolution during Directed Energy Deposition Additive Manufacturing of Ti-6Al-4V. J. Manuf. Sci. Eng. Trans. ASME. https://doi.org/10.1115/1.4038894

Bonatti, C., Mohr, D., 2017. Large deformation response of additively-manufactured FCC metamaterials: From octet truss lattices towards continuous shell mesostructures. Int. J. Plast. 92, 122–147. https://doi.org/10.1016/j.ijplas.2017.02.003

Bronkhorst, C.A., Mayeur, J.R., Livescu, V., Pokharel, R., Brown, D.W., Gray, G.T., 2019. Structural representation of additively manufactured 316L austenitic stainless steel. Int. J. Plast. 118, 70–86. https://doi.org/10.1016/j.ijplas.2019.01.012

Carroll, B.E., Palmer, T.A., Beese, A.M., 2015. Anisotropic tensile behavior of Ti-6Al-4V components fabricated with directed energy deposition additive manufacturing. Acta Mater. 87, 309–320. https://doi.org/10.1016/j.actamat.2014.12.054

Chen, L., James Edwards, T.E., Di Gioacchino, F., Clegg, W.J., Dunne, F.P.E., Pham, M.S., 2019. Crystal plasticity analysis of deformation anisotropy of lamellar TiAl alloy: 3D microstructure-based modelling and in-situ microcompression. Int. J. Plast. 119, 344–360. https://doi.org/10.1016/j.ijplas.2019.04.012

Chen, S., Xu, Y., Jiao, Y., 2018. A hybrid finite-element and cellular-automaton framework for modeling 3D microstructure of Ti-6Al-4V alloy during solid-solid phase transformation in additive manufacturing. Model. Simul. Mater. Sci. Eng. https://doi.org/10.1088/1361-651X/aabcad

Cheng, B., Price, S., Lydon, J., Cooper, K., Chou, K., 2014. On Process Temperature in Powder-Bed Electron Beam Additive Manufacturing: Model Development and Validation. J. Manuf. Sci. Eng. Trans. ASME. https://doi.org/10.1115/1.4028484

Crawford, G.A., Chawla, N., 2009. Tailoring TiO2 nanotube growth during anodic oxidation by crystallographic orientation of Ti. Scr. Mater. 60, 874–877. https://doi.org/10.1016/j.scriptamat.2009.01.043

DebRoy, T., Wei, H.L., Zuback, J.S., Mukherjee, T., Elmer, J.W., Milewski, J.O., Beese, A.M., Wilson-Heid, A., De, A., Zhang, W., 2018. Additive manufacturing of metallic components – Process, structure and properties. Prog. Mater. Sci. 92, 112–224. https://doi.org/10.1016/j.pmatsci.2017.10.001

Edwards, T.E.J., Di Gioacchino, F., Clegg, W.J., 2019. An experimental study of the polycrystalline plasticity of lamellar titanium aluminide. Int. J. Plast. 118, 291–319. https://doi.org/10.1016/j.ijplas.2019.02.013

Facchini, L., Magalini, E., Robotti, P., Molinari, A., 2009. Microstructure and mechanical properties of Ti-6Al-4V produced by electron beam melting of pre-alloyed powders. Rapid Prototyp. J. 15, 171–178. https://doi.org/10.1108/13552540910960262

Fang, Q., Chen, Y., Li, J., Jiang, C., Liu, B., Liu, Y., Liaw, P.K., 2019. Probing the phase transformation and dislocation evolution in dual-phase high-entropy alloys. Int. J. Plast. https://doi.org/10.1016/j.ijplas.2018.10.014

Filip, R., Kubiak, K., Ziaja, W., Sieniawski, J., 2003. The effect of microstructure on the mechanical properties of two-phase titanium alloys, in: Journal of Materials Processing Technology. pp. 84–89. https://doi.org/10.1016/S0924-0136(02)00248-0

Galarraga, H., Warren, R.J., Lados, D.A., Dehoff, R.R., Kirka, M.M., Nandwana, P., 2017. Effects of heat treatments on microstructure and properties of Ti-6Al-4V ELI alloy fabricated by electron beam melting (EBM). Mater. Sci. Eng. A 685, 417–428. https://doi.org/10.1016/j.msea.2017.01.019

Ge, P., Zhang, Z., Tan, Z.J., Hu, C.P., Zhao, G.Z., Guo, X., 2019. An integrated modeling of process-structure-property relationship in laser additive manufacturing of duplex titanium alloy. Int. J. Therm. Sci.

https://doi.org/10.1016/j.ijthermalsci.2019.03.013

Gil, F.J., Manero, J.M., Ginebra, M.P., Planell, J.A., 2003. The effect of cooling rate on the cyclic deformation of β-annealed Ti-6Al-4V. Mater. Sci. Eng. A 349, 150–155. https://doi.org/10.1016/S0921-5093(02)00784-0

Gil, F.J., Planell, J.A., 2000. Behaviour of normal grain growth kinetics in single phase titanium and titanium alloys. Mater. Sci. Eng. A 283, 17–24. https://doi.org/10.1016/S0921-5093(00)00731-0

Harun, W.S.W., Kamariah, M.S.I.N., Muhamad, N., Ghani, S.A.C., Ahmad, F., Mohamed, Z., 2018. A review of powder additive manufacturing processes for metallic biomaterials. Powder Technol. 327, 128–151. https://doi.org/10.1016/j.powtec.2017.12.058

Jamshidinia, M., Kong, F., Kovacevic, R., 2013. Numerical Modeling of Heat Distribution in the Electron Beam Melting ® of Ti-6Al-4V. J. Manuf. Sci. Eng. 135, 061010. https://doi.org/10.1115/1.4025746

Ji, Y., Chen, L., Chen, L.Q., 2017. Understanding Microstructure Evolution During Additive Manufacturing of Metallic Alloys Using Phase-Field Modeling, in: Thermo-Mechanical Modeling of Additive Manufacturing. pp. 93–116. https://doi.org/10.1016/B978-0-12-811820-7.00008-2

Juechter, V., Scharowsky, T., Singer, R.F., Körner, C., 2014. Processing window and evaporation phenomena for Ti-6Al-4V produced by selective electron beam melting. Acta Mater. https://doi.org/10.1016/j.actamat.2014.05.037

Katzarov, I., Malinov, S., Sha, W., 2002. Finite element modeling of the morphology of β to α phase transformation in Ti-6Al-4V alloy. Metall. Mater. Trans. A Phys. Metall. Mater. Sci. https://doi.org/10.1007/s11661-002-0204-4

Keist, J.S., Palmer, T.A., 2016. Role of geometry on properties of additively manufactured Ti-6Al-4V structures fabricated using laser based directed energy deposition. Mater. Des. https://doi.org/10.1016/j.matdes.2016.05.045

Khan, A.S., Yu, S., 2012. Deformation induced anisotropic responses of Ti-6Al-4V alloy. Part I: Experiments. Int. J. Plast. 38, 14–26. https://doi.org/10.1016/j.ijplas.2012.03.015

Khan, A.S., Yu, S., Liu, H., 2012. Deformation induced anisotropic responses of Ti-6Al-4V alloy Part II: A strain rate and temperature dependent anisotropic yield criterion. Int. J. Plast. 38, 1–13. https://doi.org/10.1016/j.ijplas.2012.03.013

Klusemann, B., Bambach, M., 2018. Stability of phase transformation models for Ti-6Al-4V under cyclic thermal loading imposed during laser metal deposition, in: AIP Conference Proceedings. https://doi.org/10.1063/1.5035004

Kochmann, J., Wulfinghoff, S., Ehle, L., Mayer, J., Svendsen, B., Reese, S., 2018. Efficient and accurate two-scale FE-FFT-based prediction of the effective material behavior of elasto-viscoplastic polycrystals. Comput. Mech. 61, 751–764. https://doi.org/10.1007/s00466-017-1476-2

Kochmann, J., Wulfinghoff, S., Reese, S., Mianroodi, J.R., Svendsen, B., 2016. Two-scale FE-FFT- and phase-field-based computational modeling of bulk microstructural evolution and macroscopic material behavior. Comput. Methods Appl. Mech. Eng. 305, 89–110. https://doi.org/10.1016/j.cma.2016.03.001

Körner, C., 2016. Additive manufacturing of metallic components by selective electron beam melting - A review. Int. Mater. Rev. https://doi.org/10.1080/09506608.2016.1176289

Krill III, C.E., Chen, L.-Q., 2002. Computer simulation of 3-D grain growth using a phase-field model. Acta Mater. 50, 3059–3075. https://doi.org/10.1016/S1359-6454(02)00084-8

Lebensohn, R.A., Kanjarla, A.K., Eisenlohr, P., 2012. An elasto-viscoplastic formulation based on fast Fourier transforms for the prediction of micromechanical fields in polycrystalline materials. Int. J. Plast. 32–33, 59–69. https://doi.org/10.1016/j.ijplas.2011.12.005

Lebensohn, R.A., Tomé, C.N., Castañeda, P.P., 2007. Self-consistent modelling of the mechanical behaviour of viscoplastic polycrystals incorporating intragranular field fluctuations. Philos. Mag. 87, 4287–4322. https://doi.org/10.1080/14786430701432619

Lee, D.N., Kim, K.H., Lee, Y.G., Choi, C.H., 1997. Factors determining crystal orientation of dendritic growth during solidification. Mater. Chem. Phys. 47, 154–158. https://doi.org/10.1016/S0254-0584(97)80044-2

Liu, P., Cui, X., Deng, J., Li, S., Li, Z., Chen, L., 2019a. Investigation of thermal responses during metallic additive manufacturing using a " Tri-Prism " finite element method. Int. J. Therm. Sci. 136, 217–229. https://doi.org/10.1016/j.ijthermalsci.2018.10.022

Liu, P., Wang, Z., Xiao, Y., Horstemeyer, M.F., Cui, X., Chen, L., 2019b. Insight into the mechanisms of columnar to equiaxed grain transition during metallic additive manufacturing. Addit. Manuf. 26, 22–29.

Liu, P.W., Ji, Y.Z., Wang, Z., Qiu, C.L., Antonysamy, A.A., Chen, L.Q., Cui, X.Y., Chen, L., 2018. Investigation on evolution mechanisms of site-specific grain structures during metal additive manufacturing. J. Mater. Process. Technol. 257, 191–202. https://doi.org/10.1016/j.jmatprotec.2018.02.042

Liu, R., Wang, Z., Sparks, T., Liou, F., Newkirk, J., 2016. Aerospace applications of laser additive manufacturing, in: Laser Additive Manufacturing: Materials, Design, Technologies, and Applications. https://doi.org/10.1016/B978-0-08-100433-3.00013-0

Mainprice, D., Hielscher, R., Schaeben, H., 2011. Calculating anisotropic physical properties from texture data using the MTEX open source package. Society.

Malinov, S., Sha, W., 2005. Modeling thermodynamics, kinetics, and phase transformation morphology while heat treating titanium alloys. JOM. https://doi.org/10.1007/s11837-005-0114-1

Mandal, S., Gockel, B.T., Balachandran, S., Banerjee, D., Rollett, A.D., 2017. Simulation of plastic deformation in Ti-5553 alloy using a self-consistent viscoplastic model. Int. J. Plast. 94, 57–73. https://doi.org/10.1016/j.ijplas.2017.02.008

Martin, J.H., Yahata, B.D., Hundley, J.M., Mayer, J.A., Schaedler, T.A., Pollock, T.M., 2017. 3D printing of high-strength aluminium alloys. Nature 549, 365–369. https://doi.org/10.1038/nature23894

Michel, J. C., H. Moulinec, and P.S., 2000. A computational method based on augmented lagrangians and fast fourier transforms for composites with high contrast. C. - Comput. Model. Eng. Sci. 1, 79–88. https://doi.org/10.3970/cmes.2000.001.239

Murgau, C.C., 2016. Microstructure Model for Ti-6Al-4V used in Simulation of Additive Manufacturing. LuleÅ University of Technology.

Murgau, C.C., Pederson, R., Lindgren, L.E., 2012. A model for Ti6Al4V microstructure evolution for arbitrary temperature changes. Model. Simul. Mater. Sci. Eng. https://doi.org/10.1088/0965-0393/20/5/055006

Ohno, M., Yamaguchi, T., Sato, D., Matsuura, K., 2013. Existence or nonexistence of thermal pinning effect in grain growth under temperature gradient. Comput. Mater. Sci. 69, 7–13. https://doi.org/10.1016/j.commatsci.2012.11.017

Ozturk, T., Rollett, A.D., 2018. Effect of microstructure on the elasto-viscoplastic deformation of dual phase titanium structures. Comput. Mech. 61, 55–70. https://doi.org/10.1007/s00466-017-1467-3

Palanivel, S., Dutt, A.K., Faierson, E.J., Mishra, R.S., 2016. Spatially dependent properties in a laser additive manufactured Ti-6Al-4V component. Mater. Sci. Eng. A. https://doi.org/10.1016/j.msea.2015.12.021

Qiu, C., Adkins, N.J.E., Attallah, M.M., 2013. Microstructure and tensile properties of selectively laser-melted and of HIPed laser-melted Ti-6Al-4V. Mater. Sci. Eng. A 578, 230–239. https://doi.org/10.1016/j.msea.2013.04.099

Qiu, C., Panwisawas, C., Ward, M., Basoalto, H.C., Brooks, J.W., Attallah, M.M., 2015. On the role of melt flow into the surface structure and porosity development during selective laser melting. Acta Mater. 96, 72–79. https://doi.org/10.1016/j.actamat.2015.06.004

Rafi, H.K., Karthik, N. V., Gong, H., Starr, T.L., Stucker, B.E., 2013a. Microstructures and mechanical properties of Ti6Al4V parts fabricated by selective laser melting and electron beam melting. J. Mater. Eng. Perform. 22, 3872–3883. https://doi.org/10.1007/s11665-013-0658-0

Rafi, H.K., Starr, T.L., Stucker, B.E., 2013b. A comparison of the tensile, fatigue, and fracture behavior of Ti-6Al-4V and 15-5 PH stainless steel parts made by selective laser melting. Int. J. Adv. Manuf. Technol. https://doi.org/10.1007/s00170-013-5106-7

Raghavan, N., Dehoff, R., Pannala, S., Simunovic, S., Kirka, M., Turner, J., Carlson, N., Babu, S.S., 2016. Numerical modeling of heat-transfer and the influence of process parameters on tailoring the grain morphology of IN718 in electron beam additive manufacturing. Acta Mater. 112, 303–314. https://doi.org/10.1016/j.actamat.2016.03.063

Sahoo, S., Chou, K., 2016. Phase-field simulation of microstructure evolution of Ti-6Al-4V in electron beam additive manufacturing process. Addit. Manuf. 9, 14–24. https://doi.org/10.1016/j.addma.2015.12.005

Scharowsky, T., Juechter, V., Singer, R.F., Körner, C., 2015. Influence of the Scanning Strategy on the Microstructure and Mechanical Properties in Selective Electron Beam Melting of Ti-6Al-4V. Adv. Eng. Mater. 17, 1573–1578. https://doi.org/10.1002/adem.201400542

Schempp, P., Cross, C.E., Pittner, A., Oder, G., Neumann, R.S., Rooch, H., Dörfel, I., Österle, W., Rethmeier, M., 2014. Solidification of GTA aluminum weld metal: Part I - Grain morphology dependent upon alloy composition and grain refiner content. Weld. J. 93, 53s-59s.

Schwarzer, R.A., Gerth, D., 1993. The effect of grain orientation on the relaxation of thermomechanical stress and hillock growth in AI-1%Si conductor layers on silicon substrates. J. Electron. Mater. 22, 607–610. https://doi.org/10.1007/BF02666405

Shewchuk, J.R., 2002. What is a good linear finite element? interpolation, conditioning, anisotropy, and quality measures (preprint). Univ. Calif. Berkeley.

Sidambe, A.T., 2014. Biocompatibility of advanced manufactured titanium implants-A review. Materials (Basel). 7, 8168–8188. https://doi.org/10.3390/ma7128168

Sieniawski, J., Ziaja, W., Kubiak, K., Motyk, M., 2013. Microstructure and Mechanical Properties of High Strength Two-Phase Titanium Alloys, in: Titanium Alloys - Advances in Properties Control. https://doi.org/10.5772/56197

Socrates, G., 2003. Texture analysis in materials science - 2Ed, Materials & Design. Elsevier. https://doi.org/10.1016/0261-3069(83)90207-8

Systèmes, D., 2018. Abaqus 2018.

Tan, X., Kok, Y., Tan, Y.J., Descoins, M., Mangelinck, D., Tor, S.B., Leong, K.F., Chua, C.K., 2015. Graded microstructure and mechanical properties of additive manufactured Ti-6Al-4V via electron beam melting. Acta Mater. 97, 1–16. https://doi.org/10.1016/j.actamat.2015.06.036

Tancogne-Dejean, T., Roth, C.C., Woy, U., Mohr, D., 2016. Probabilistic fracture of Ti-6Al-4V made through additive layer manufacturing. Int. J. Plast. 78, 145–172. https://doi.org/10.1016/j.ijplas.2015.09.007

Tari, V., Lebensohn, R.A., Pokharel, R., Turner, T.J., Shade, P.A., Bernier, J. V., Rollett, A.D., 2018. Validation of micro-mechanical FFT-based simulations using High Energy Diffraction Microscopy on Ti-7Al. Acta Mater. 154, 273–283. https://doi.org/10.1016/j.actamat.2018.05.036

Thomas, J., Groeber, M., Ghosh, S., 2012. Image-based crystal plasticity FE framework for microstructure dependent properties of Ti-6Al-4V alloys. Mater. Sci. Eng. A 553, 164–175. https://doi.org/10.1016/j.msea.2012.06.006

Tome, C., Canova, G.R., Kocks, U.F., Christodoulou, N., Jonas, J.J., 1984. The relation between macroscopic and microscopic strain hardening in F.C.C. polycrystals. Acta Metall. 32, 1637–1653. https://doi.org/10.1016/0001-6160(84)90222-0

Wang, P., Tan, X., Nai, M.L.S., Tor, S.B., Wei, J., 2016. Spatial and geometrical-based characterization of microstructure and microhardness for an electron beam melted Ti-6Al-4V component. Mater. Des. 95, 287–295. https://doi.org/10.1016/j.matdes.2016.01.093

Wang, X., Liu, P.W., Ji, Y., Liu, Y., Horstemeyer, M.H., Chen, L., 2019. Investigation on Microsegregation of IN718 Alloy During Additive Manufacturing via Integrated Phase-Field and Finite-Element Modeling. J. Mater. Eng. Perform. 28, 657–665. https://doi.org/10.1007/s11665-018-3620-3

Wang, Z., Liu, P., Ji, Y., Mahadevan, S., Horstemeyer, M.F., Hu, Z., Chen, L., Chen, L.Q., 2019a. Uncertainty Quantification in Metallic Additive Manufacturing Through Physics-Informed Data-Driven Modeling. JOM. https://doi.org/10.1007/s11837-019-03555-z

Wang, Z., Liu, P., Xiao, Y., Cui, X., Hu, Z., Chen, L., 2019b. A Data-Driven Approach for Process Optimization of Metallic Additive Manufacturing under Uncertainty. J. Manuf. Sci. Eng. Trans. ASME. https://doi.org/10.1115/1.4043798

Wei, H.L., Knapp, G.L., Mukherjee, T., DebRoy, T., 2019. Three-dimensional grain growth during multi-layer printing of a nickel-based alloy Inconel 718. Addit. Manuf. 25, 448–459. https://doi.org/10.1016/j.addma.2018.11.028

Williams, J.C., Starke, E.A., 2003. Progress in structural materials for aerospace systems. Acta Mater. 51, 5775–5799. https://doi.org/10.1016/j.actamat.2003.08.023

Wilson-Heid, A.E., Wang, Z., McCornac, B., Beese, A.M., 2017. Quantitative relationship between anisotropic strain to failure and grain morphology in additively manufactured Ti-6Al-4V. Mater. Sci. Eng. A 706, 287–294. https://doi.org/10.1016/j.msea.2017.09.017

Xu, W., Brandt, M., Sun, S., Elambasseril, J., Liu, Q., Latham, K., Xia, K., Qian, M., 2015. Additive manufacturing of strong and ductile Ti-6Al-4V by selective laser melting via in situ martensite decomposition. Acta Mater. https://doi.org/10.1016/j.actamat.2014.11.028

Yan, W., Ge, W., Qian, Y., Lin, S., Zhou, B., Liu, W.K., Lin, F., Wagner, G.J., 2017. Multi-physics modeling of single/multiple-track defect mechanisms in electron beam selective melting. Acta Mater. 134, 324–333. https://doi.org/10.1016/j.actamat.2017.05.061

Yan, W., Lian, Y., Yu, C., Kafka, O.L., Liu, Z., Liu, W.K., Wagner, G.J., 2018a. An integrated process–structure–property modeling framework for additive manufacturing. Comput. Methods Appl. Mech. Eng. 339, 184–204. https://doi.org/10.1016/j.cma.2018.05.004

Yan, W., Qian, Y., Ge, W., Lin, S., Liu, W.K., Lin, F., Wagner, G.J., 2018b. Meso-scale modeling of multiple-layer fabrication process in Selective Electron Beam Melting: Inter-layer/track voids formation. Mater. Des. 141, 210–219. https://doi.org/10.1016/j.matdes.2017.12.031

Zhang, M., Zhang, J., McDowell, D.L., 2007. Microstructure-based crystal plasticity modeling of cyclic deformation of Ti-6Al-4V. Int. J. Plast. 23, 1328–1348. https://doi.org/10.1016/j.ijplas.2006.11.009

Zhang, Z., Yao, X.X., Ge, P., 2019. Phase-field-model-based analysis of the effects of powder particle on porosities and densities in selective laser sintering additive manufacturing. Int. J. Mech. Sci. In Press.

Zhao, X., Li, S., Zhang, M., Liu, Y., Sercombe, T.B., Wang, S., Hao, Y., Yang, R., Murr, L.E., 2016. Comparison of the microstructures and mechanical properties of Ti-6Al-4V fabricated by selective laser melting and electron beam melting. Mater. Des. https://doi.org/10.1016/j.matdes.2015.12.135

Figure captions

Fig. 1. Schematic of the proposed multiscale computational framework to investigate the process-microstructure-property relationship of AM-fabricated metallic material. Some directly relative parameters/ variables that required to be transferred between different models are listed. They include high temperature field $\boldsymbol{T}$, beam power P, scanning speed v, hatching space h_s, layer thickness t_l, cooling rate, volume fraction of α-phase V_f, α-lath thickness t_α and lamellar α+β microstructure and so on.

Fig. 2. (a) A typical schematic of powder bed-based electron beam melting process. Γ_1 shows the domain on which Dirichlet boundary condition is applied. The convection and radiation boundary conditions are applied on the top surface of the printed parts Γ_2. (b) plots the thermal conductivities of the printed part k and powders k_{powder} at different temperature.

Fig. 3. (a) Schematic of grain nucleation and growth near the melt pool. v and R are scanning speed of electron beam and solidification rate, respectively, L and S represent liquidus and solidus. The mushy zone involves both liquid and solid phases, (b) and (c) plot the hypothetical solute concentration and corresponding temperature profile near the S/L interface. The horizontal axis describes the distance from the grain front along solidification direction. θ, the slope of the line of actual temperature, is equal to the thermal gradient.

Fig. 4. (a) and (b) show the scanning electron microscope (SEM) results (Tan et al., 2015), including the columnar prior β-grains and colony morphologies, i.e., lamellar α+β microstructures within prior β-grains. As α-phase was etched out by Kroll's reagent, it exhibits dark contrast while β is in bright under SEM mode; (c) demonstrates a representative schematic of the lamellar α+β microstructure, which is composed of the successive parallel α- and β-phases. t_α and t_β are the thicknesses of α- and β-laths; (d) a simulated 3D lamellar α+β microstructure.

Fig. 5. 3D β-grain morphologies, involving (a) columnar grains and (b) equiaxed grains. (a)

and (b) display the results simulated by the grain growth phase-field model under processing condition 1 and processing condition 2, respectively; (c) and (d) display the transformed lamellar α+β microstructures that are cut directly from (a) and (b), respectively, and then used for EVP-FFT calculations.

Fig. 6. Diagram showing the transition of β-grain structures as a function of the solidification rate R and the thermal gradient G. Two fitted boundary lines from computational data points represented by the symbols, with purple, dark green and blue colors, divide the grain-structure region into three different zones, i.e., columnar, mixed and equiaxed zones, respectively. The red rectangle shows the ranges of solidification parameters, i.e., thermal gradient and solidification rate, with the common experimental conditions. The inserted 3D plot shows the simulated thermal gradient in the range of $1.0 \sim 3.0 \times 10^6$ K/m under the printing conditions of P = 480 W, v: 0.2 ~ 0.8 m/s, T_P: 873 ~1200 K. The red shurikens display the experimental data for AM-built Ti-6Al-4V taken from Refs. (Al-Bermani et al., 2010; Antonysamy et al., 2013; Juechter et al., 2014; Rafi et al., 2013a; Tan et al., 2015).

Fig. 7. Anisotropic mechanical properties of the large columnar grain structures under the processing condition 1.

Fig. 8. Micromechanical fields predicted in the large columnar grain structures under the processing condition 1. The white lines describe the grain boundaries. (a) and (b) show the strain and stress fields with tension applied along N_z-direction; (c) and (d) show the strain and stress fields with tension applied along R_x-direction.

Fig. 9. Elongation and yield stress ratios (N_z-direction/R_x-direction), marked by black circles and blue squares, respectively, versus grain aspect ratio (grain height, H/width, W) for tests performed in Wilson's study (Wilson-Heid et al., 2017) as well as data from literature (Carroll et al., 2015; Keist and Palmer, 2016; Palanivel et al., 2016; Qiu et al., 2013; Rafi et al., 2013a, 2013b; Zhao et al., 2016). A fitted function, manifested by the black dotted curve,

is obtained from the experimental data, which is further used to calculate the elongation ratios, marked by red stars, using the simulated grain aspect ratios under Processing Condition 1 and 2 (PC 1 and PC2). The green triangles demonstrate the simulated yield stress ratios under PC 1 and PC 2.

Fig. 10. Effect of different grain morphologies on mechanical properties.

Fig. 11. Micromechanical fields for the equiaxed grain structures under the processing condition 2. The white lines describe the grain boundaries. (a) and (b) show the results with tension applied along N_z-direction; (c) and (d) show the results with tension applied along R_x-direction.

Fig. A1. Pole figures of columnar β-grain textures: (a) and (b) experimental measurements and simulation results, respectively, under processing condition 1.

Fig. A2. Stress-strain curves corresponding to experiment (Facchini et al., 2009), and simulation using the proposed model.

Fig. A3. Yield stress as a function of the inverse square root of α-lath thickness.

Fig. A4. Relationships between average Von-Mises stress and volume fraction of α-phase.

COLLEGE OF
ENGINEERING & COMPUTER SCIENCE
UNIVERSITY OF MICHIGAN-DEARBORN

We declare that this manuscript is original, has not been published before and is not currently being considered for publication elsewhere. The manuscript has been read and approved by all named authors.

2340 HPEC, 4901 Evergreen Rd.
Dearborn, Michigan 48128-2406

Tel: 313 593 5361
leichn@umich.edu